Publ. Astron. Soc. Japan (2022) 74 (1), 92–127
https://doi.org/10.1093/pasj/psab112
Advance Access Publication Date: 2021 December 22

Regular radial velocity variations in nine G- and K-type giant stars: Eight planets and one planet candidate

Huan-Yu Teng,[1,*] **Bun'ei Sato**,[1] **Takuya Takarada**,[2] **Masashi Omiya**,[2,3] **Hiroki Harakawa**,[4] **Hideyuki Izumiura**,[5] **Eiji Kambe**,[4] **Yoichi Takeda**,[6] **Michitoshi Yoshida**,[4] **Yoichi Itoh**,[7] **Hiroyasu Ando**,[3] and **Eiichiro Kokubo**[8]

[1]Department of Earth and Planetary Sciences, School of Science, Tokyo Institute of Technology, 2-12-1 Ookayama, Meguro-ku, Tokyo 152-8551, Japan
[2]Astrobiology Center, National Institutes of Natural Sciences, 2-21-1 Osawa, Mitaka, Tokyo 181-8588, Japan
[3]National Astronomical Observatory of Japan, National Institutes of Natural Sciences, 2-21-1 Osawa, Mitaka, Tokyo 181-8588, Japan
[4]Subaru Telescope, National Astronomical Observatory of Japan, National Institutes of Natural Sciences, 650 North A'ohoku Pl., Hilo, HI 96720, USA
[5]Okayama Branch Office, Subaru Telescope, National Astronomical Observatory of Japan, National Institute of Natural Sciences, Kamogata, Asakuchi, Okayama 719-0232, Japan
[6]11-2 Enomachi, Naka-ku, Hiroshima-shi, Hiroshima 730-0851, Japan
[7]Nishi-Harima Astronomical Observatory, Center for Astronomy, University of Hyogo, 407-2 Nishigaichi, Sayo, Hyogo 679-5313, Japan
[8]The Graduate University for Advanced Studies (SOKENDAI), 2-21-1 Osawa, Mitaka, Tokyo 181-8588, Japan

*E-mail: teng.h.aa@m.titech.ac.jp

Received 2021 June 15; Accepted 2021 November 8

Abstract

We report the detection of radial velocity (RV) variations in nine evolved G- and K-type giant stars. The observations were conducted at Okayama Astrophysical Observatory. Planets or planet candidates can best explain these regular variations. However, a coincidence of near 280 d variability among five of them prevents us from fully ruling out stellar origins for some of the variations, since all nine stars behave similarly in stellar properties. In the planet hypotheses for the RV variations, the planets (including one candidate) may survive close to the boundary of the so-called "planet desert" around evolved stars, having orbital periods between 255 and 555 d. Besides, they are the least-massive giant planets detected around G- and K-type giant stars, with minimum masses between 0.45 M_J and 1.34 M_J. We further investigated other hypotheses for our detection, yet none of them can better explain regular RV variation. With our detection, we can be convinced that year-long regular variation with amplitude down to 15 m s^{-1} for G- and K-type giant stars is detectable. Moreover, we performed simulations to further confirm the detectability of planets around these stars. Finally, we explored giant planets around

© The Author(s) 2021. Published by Oxford University Press on behalf of the Astronomical Society of Japan.
All rights reserved. For permissions, please e-mail: journals.permissions@oup.com

intermediate-mass stars, and likewise found a four-Jupiter-mass gap (e.g., Santos et al. 2017, A&A, 603, A30), which is probably a boundary of the giant planet population.

Key words: planetary systems — stars: individual (HD 360, ϵ Piscium, HD 10975, HD 79181, HD 99283, υ Leo, HD 161178, HD 219139, γ Piscium) — techniques: radial velocities

1 Introduction

Since the first extrasolar planet (exoplanet) 51 Peg b was detected, more than 4000 exoplanets in 3000 planetary systems have been discovered around different types of stars. These exoplanets were detected by different methods, among which the radial velocity (RV) method (Doppler method) contributed nearly 800 of them. For these planets, about 60% are detected around solar-mass (0.7–1.5 $M_\odot$) stars, while only about 1% are detected around intermediate-mass (1.5–5.0 $M_\odot$) stars because of the difficulty in detecting planets around them. However, since the properties such as mass and lifetime of the circumstellar disks around intermediate-mass stars are different from those around solar-mass and low-mass stars (Haisch et al. 2001a, 2001b; Andrews et al. 2013; Ribas et al. 2015), intermediate-mass stars are valuable observational objects in terms of constraining the mechanism and timescale of planet formation. Currently, there are two plausible scenarios to solve the puzzle; the core accretion scenario (e.g., Safronov 1969; Goldreich & Ward 1973; Hayashi et al. 1985; Pollack et al. 1996) and the disk instability scenario (e.g., Kuiper 1951; Cameron 1978). Therefore, more observational evidence becomes urgent in understanding when different procedures apply in giant planet formation.

To observe intermediate-mass stars, it is usually hard to search for planets with the RV method around the main sequence (MS) stars. This is because intermediate-mass MS stars exhibit few absorption lines due to their high surface temperature and fast self-rotation (Lagrange et al. 2009), while evolved intermediate-mass stars, which are the evolved counterparts of late-F to early-B dwarfs and spectroscopically G- or K-type subgiants or giants, have lower temperatures and slower rotation, which is more appropriate for RV measurements. So far, several groups have been surveying these evolved intermediate-mass stars with the RV method: the Okayama Planet Search Program (Sato et al. 2005) and its collaborative survey "EAPS-Net" (Izumiura 2005), the BOAO K-giant survey (Han et al. 2010), the Lick G- and K-giant survey (Frink et al. 2001; Hekker et al. 2006), the ESO planet search program (Setiawan et al. 2003), the Tautenburg Observatory Planet Search (Hatzes et al. 2005; Döllinger et al. 2007), the Penn State Toruń Planet Search (Niedzielski et al. 2007) and its RV follow-up program Tracking Advanced Planetary Systems (Niedzielski et al. 2015), the survey "Retired A Stars and Their Companions" (Johnson et al. 2006), the Pan-Pacific Planet Search (Wittenmyer et al. 2011), and the EXoPlanet aRound Evolved StarS project (Jones et al. 2011). Thanks to these large-scale surveys, around 150 planets have been discovered around evolved stars.

An interesting problem of a "planet desert" happened to these evolved intermediate-mass stars; namely, close-in ($a < 0.6$ au), low-mass ($M_\mathrm{p} < 0.6 M_\mathrm{J}$) planets were seldom found (Johnson et al. 2007; Lillo-Box et al. 2016; Medina et al. 2018). Thanks to precise RV measurements and transiting observations (e.g., the Kepler space telescope Borucki et al. 2012), few planets with semi-major axes and minimum masses lower than 0.1 au and 0.1 M_J, respectively, have been discovered around intermediate-mass evolved stars (Huber et al. 2013; Johnson et al. 2010). Especially for evolved giant stars, most detected planets reside at more than 0.5 au from their hosts (Jones et al. 2014). According to a simulation given by Alibert, Mordasini, and Benz (2011), the desert could be attributed to a scaling of the proto-planetary disk mass with the mass of the central star. Nevertheless, when the mass of a central star is getting lower, a few warm planets less massive than 1 M_J could survive around or closer than 1 au from their central stars. Therefore, observing intermediate-mass stars could be a key point in constraining the mass relation between the proto-planetary disk and the central star. In addition, among all detected giant exoplanets, they are more likely to reside around metal-rich stars. However, specifically for these evolved stars, many studies give the same planet–metallicity correlation, i.e., they all prefer high metallicities (e.g., Reffert et al. 2015; Jones et al. 2016; Wittenmyer et al. 2017a), while some others (e.g., Jofré et al. 2015) give no clear correlation. In up-to-date research given by Santos et al. (2017), the distribution of giant planet companions is likely to present more than one population with a change in regime around 4 M_J, above which host stars tend to be more metal-poor and more massive. On the other hand, stars hosting planets below this limit show the well-known metallicity–giant planet frequency correlation. In other words, the giant planet–metallicity correlation around evolved stars still needs improvement.

In this work, we study nine evolved G- and K-type giant stars that emerged from the Okayama Planet Search

Program (Sato et al. 2005). These nine stars exhibit RV amplitude of only a few tens of meters per second, and five of these stars coincidentally show regular RV variations at nearly 280 d. According to our investigation, these variations are best explained by planet nature, yet we could not fully rule out the stellar origin of the 280 d variability. The rest of this paper is organized as follows. The observations are described in section 2 and the stellar properties are described in section 3. In section 4, we make a detailed presentation of our analysis of RV measurements, line profile and chromospheric activity, period search, and Keplerian orbital fit. In section 5, we show our Keplerian fitting results by stars. Finally, in section 6 we present discussions about alternative explanations and then summarize the paper. In addition, detailed analyses on IP variability, instrumental stability, and individual stars are given in appendices 1, 2, and 3, respectively.

2 Observations

In this work, all spectra of the nine stars (HD 360, ϵ Psc, HD 10975, HD 79181, HD 99283, υ Leo, HD 161178, HD 219139, and γ Psc) were obtained by the 1.88 m reflector with the HIgh Dispersion Echelle Spectrograph (HIDES: Izumiura 1999) at the Okayama Astrophysical Observatory. The first spectrum was obtained in 2001 under the Okayama Planet Search Program (Sato et al. 2005), which focuses on radial velocity measurements to late-G (or early-K) giant stars, and aims at opening the world of planets around intermediate-mass stars. As for the instrument, an iodine cell was placed in the HIDES optical path, which provided numerous iodine absorption lines in the range of 5000–5800 Å as a reference for precise radial velocity measurements. To cover these iodine absorption lines, the wavelength region of HIDES was firstly set to cover 5000–6100 Å with one 2K × 4K CCD. In 2007 December, the CCD of HIDES was upgraded from the single one to a mosaic of three, which widened the wavelength region to 3700–7500 Å (3700–5000 Å, 5000–5800 Å, and 5800–7500 Å for each respectively). The upgrade enabled us to measure the level of stellar activities simultaneously (e.g., Ca II HK lines) and line profiles as well as radial velocities. In 2010, a new high-efficiency fiber-link system with its own iodine cell was installed to the HIDES which greatly enhanced the overall throughput (Kambe et al. 2013). In this research, the spectra were obtained by both conventional slit mode with CCD pre- and post-upgrade (hereafter HIDES-S), and fiber-link mode (hereafter HIDES-F).

In the case of HIDES-S observations, the slit width was set to 200 μm ($0\farcs76$) corresponding to the resolution $R = \lambda/\Delta\lambda \sim 67000$ by about 3.3 pixel sampling. In the case of HIDES-F observations, the width of the sliced image was $1\farcs05$ corresponding to the resolution $R \sim 55000$ by about 3.8 pixel sampling. There was an offset in radial velocity measurements between two modes due to the respective iodine in their optical paths, hence we treated two modes as two different instruments in our research.

We adopted the data which gained signal-to-noise ratios (S/N) over approximately 100 per pixel at ∼5500 Å within 1800 s. For the faintest star (HD 10975, $V = 5.93$) in this work, the typical exposure time and S/N is 1200 s and over 150, and 500 s over 200, in the case of HIDES-S and HIDES-F observations respectively.

The reduction of these echelle spectra (i.e., bias subtraction, flat-fielding, scattered light subtraction, and spectrum extraction) was performed with IRAF packages in a standard way.footnoteIRAF is distributed by the National Optical Astronomy Observatories, which is operated by the Association of Universities for Research in Astronomy, Inc. under a cooperative agreement with the National Science Foundation, USA In particular, for HIDES-F spectra there were severe aperture overlaps among 3700–4000 Å owing to the use of an image slicer, therefore the scattered light for these apertures could not be subtracted with IRAF task `apscatter`. Consequently, we discard these overlapped apertures and did not analyze the Ca II H lines for HIDES-F spectra.

3 Stellar properties

The nine stars in this research include HD 360, ϵ Psc, HD 10975, HD 79181, HD 99283, υ Leo, HD 161178, HD 219139, and γ Psc. We collected spectral type and V-band magnitudes from the Hipparcos catalog (ESA 1997), and we collect parallax from either Hipparcos (ESA: van Leeuwen 2007) or Gaia EDR3 (Gaia Collaboration 2016, 2020; Lindegren et al. 2021) according to precision. The atmospheric parameters (effective temperature $T_{\mathrm{eff,sp}}$, surface gravity $\log g_{\mathrm{sp}}$, and Fe abundance $[\mathrm{Fe/H}]_{\mathrm{sp}}$) were determined by Takeda, Sato, and Murata (2008) by measuring the equivalent width of Fe I and Fe II lines of iodine-free stellar spectra. Takeda, Sato, and Murata (2008) also determined the projected rotational velocity, $v\sin i$, with the automatic spectrum-fitting technique (Takeda 1995).

However, according to work by Takeda and Tajitsu (2015), stellar masses in Takeda, Sato, and Murata (2008) tend to be overestimated by up to a factor of $\lesssim 2$, especially for giant stars located near the red clump regions in the Hertzsprung–Russell (HR) diagram. For this reason, we re-estimated stellar parameters by adopting the Bayesian estimation method with theoretical isochrones with isoclassify (Huber et al. 2017; Berger et al. 2020). Using the isoclassify "direct" mode, $R_\star$ and $L_\star$ were calculated from posterior probability distributions by applying the Stefan–Boltzmann law with spectroscopic $T_{\mathrm{eff,sp}}$ and V-band as photometry as inputs. In this step, distances were sampled following the parallax a posterior from either Hipparcos or Gaia EDR3. For each distance sample, the extinction A_V was calculated with map given by Green et al. (2019) as implemented in mwdust package by Bovy et al. (2016). Each sample was combined with independent random normal samples for apparent magnitude and effective temperature T_{eff}. The bolometric corrections were derived by linearly interpolating T_{eff}, [Fe/H], $\log g_\star$, and A_V in the MESA Isochrones & Stellar Tracks (MIST)/C3K grid (C. Conroy et al. in preparation).[1] The derived distances, extinctions, and bolometric corrections were iterated until convergence. Using the isoclassify "grid" mode, parameters including T_{eff}, [Fe/H], $\log g_\star$, $L_\star$, $R_\star$, and $M_\star$ were estimated with posterior distribution by integrating over the MIST isochrone (Paxton et al. 2011, 2013, 2015, 2018; Choi et al. 2016; Dotter 2016). Consequently, with masses estimated, some stars were re-classified as solar-mass stars, or namely, low-mass giant stars. The properties of the nine stars in this paper are listed in table 1 and plotted on the HR diagram in figure 1. These nine stars are known to be stable in photometry with a level of $\sigma_{\mathrm{HIP}} = 0.006$–$0.011$ mag (ESA: van Leeuwen 2007), and they are chromospherically inactive with no significant emission in the core of the Ca II H lines, as shown in figure 2. Another chromospherically active G-type giant star (HD 120048) serves as a comparison to the nine stars. It is also shown in figure 2, where we can see clear emission lines in the core of the Ca II H lines.

4 Analysis

4.1 Radial velocity

For precise RV measurements, we used spectra covering 5000 to 5800 Å in which I_2 absorption lines are superimposed by an I_2 cell. We computed RV variations following the method described in Sato et al. (2002, 2012) which was based on a method by Butler et al. (1996). We modeled the spectra (I_2 superposed stellar spectra) by using the stellar template and high-resolution I_2 spectra which were convolved with the instrumental profile (IP) of the spectrograph. IP was described as one central Gaussian envelope and 10 satellite Gaussian envelopes, where we fixed the widths of 0.9 pixel and positions of 0.9 pixel and set the height as free parameters. Further analysis of IP variability is given in appendix 1. The stellar template spectra used for HIDES-S were obtained by deconvolving pure stellar spectra with the IP estimated from I_2 superposed B-type star or flat spectra. The stellar template spectra used for HIDES-F were obtained by HIDES-F high-resolution mode ($R \sim 100000$) observations without I_2 in its optical path. RV offsets of HIDES-S and HIDES-F were set to the mean level of the full RV time series as two free parameters (see subsection 4.4). Hundreds of segments at a typical width of 150 pixel were set in the observed spectra in the I_2 absorption region, and the final RV values and their measurement errors were taken from the average of measurement in each segment. The analysis of RV stability of the instruments is given in appendix 2.

4.2 Line profile and chromospheric activity

A fake planetary signal could possibly be masqueraded by wavelength shift due to spectral line profile deformation. To evaluate this possibility, we perform line profile analyses following the same procedure in Takarada et al. (2018). The iodine-free spectra within the wavelength range of 4000–5000 are adopted for this analysis. First, we calculate the weighted cross-correlation function (CCF: Baranne et al. 1996; Pepe et al. 2002) and a numerical mask. The CCF is constructed by shifting the mask as a function of Doppler velocity, and its weight is determined by the depth of the spectral line. The numerical mask is generated from SPECTRUM (Gray & Corbally 1994) for a G-type giant star with approximately 800 lines. Next, we calculate the bisector inverse span (BIS: Dall et al. 2006) of the CCF. The BIS is defined as the offset of averaged velocity between the upper region (5%–15% from the continuum of the CCF) and the lower region (85%–95% from the continuum of the CCF). Thus, we adopt the BIS as a measurement of line-profile asymmetry. Moreover, the full width at half maximum (FWHM: e.g., Suárez Mascareño et al. 2020) of CCF for bisector by each instrument is used as another line profile indicator. In order to remove the instrumental difference between each instrument, we define $\mathrm{BIS}' = \mathrm{BIS} - \overline{\mathrm{BIS}}$, and $\mathrm{FWHM}' = \mathrm{FWHM} - \overline{\mathrm{FWHM}}$ for each instrument, where an overline represents the mean value.

Stellar chromospheric activity could be one of the explanations for RV variations. For G- and K-type stars, Ca II HK lines, the line core fluxes of which efficiently trace the chromospheric activity (Duncan et al. 1991), have been widely used as activity indicators. For HIDES, the signal-to-noise ratios of Ca II K lines are not high enough for use as the indicator. Hence, following Sato et al. (2013), we defined the Ca II H index S_H as

$$S_H = \frac{F_H}{F_B + F_R} \tag{1}$$

where F_H is a total flux in a wavelength bin 0.66 Å wide centered on the H line, and F_B and F_R are those in bins 1.1 Å wide centered on minus and plus 1.2 Å from the center of

---

[1] ⟨http://waps.cfa.harvard.edu/MIST/model_grids.html⟩.

Table 1. Stellar parameters.*

	HD 360	ϵ Psc	HD 10975	HD 79181	HD 99283	υ Leo	HD 161178	HD 219139	γ Psc	Sources
π (mas)	9.0115^{a}	17.8074^{a}	8.6049^{a}	9.6870^{a}	9.1832^{a}	18.3461^{a}	9.3052^{a}	9.4433^{a}	23.64^{b}	a, b
V	5.98	4.28	5.93	5.72	5.70	4.30	5.87	5.85	3.70	Hipparcos
$B - V$	1.03	0.96	0.99	0.97	1.00	1.01	1.02	1.00	0.92	Hipparcos
Spec. type	G8 III	K0 III	K0 III	G8 III	K0 III	G9 III	G9 III	G5 III	G7 III	Hipparcos
$T_{\mathrm{eff,\,sp}}$ (K)	4850	4829	4866	4842	4883	4835	4766	4860	4802	Takeda08
$[\mathrm{Fe/H}]_{\mathrm{sp}}$ (dex)	−0.08	−0.31	−0.17	−0.29	−0.17	−0.19	−0.20	−0.19	−0.62	Takeda08
$\log g_{\star,\mathrm{sp}}$ (cgs)	2.62	2.30	2.47	2.47	2.59	2.47	2.33	2.50	2.25	Takeda08
$v \sin i$ (km s^{-1})	1.86	1.79	1.69	1.84	1.87	1.78	1.78	2.04	1.67	Takeda08
T_{eff} (K)	4770	4824	4840	4862	4886	4836	4786	4831	4742	This work
[Fe/H] (dex)	$-0.06^{+0.17}_{-0.10}$	$-0.31^{+0.10}_{-0.10}$	$-0.21^{+0.10}_{-0.08}$	$-0.28^{+0.08}_{-0.09}$	$-0.16^{+0.06}_{-0.10}$	$-0.20^{+0.09}_{-0.08}$	$-0.21^{+0.09}_{-0.07}$	$-0.20^{+0.09}_{-0.07}$	$-0.62^{+0.10}_{-0.11}$	This work
$\log g_{\star}$ (cgs)	$2.59^{+0.05}_{-0.17}$	$2.34^{+0.07}_{-0.13}$	$2.48^{+0.09}_{-0.09}$	$2.45^{+0.09}_{-0.07}$	$2.57^{+0.07}_{-0.08}$	$2.46^{+0.09}_{-0.09}$	$2.38^{+0.07}_{-0.03}$	$2.48^{+0.08}_{-0.07}$	$2.33^{+0.08}_{-0.07}$	This work
$L_{\star}$ ($L_{\odot}$)	$55.16^{+2.14}_{-2.81}$	$75.52^{+130.72}_{-21.93}$	$61.64^{+6.80}_{-5.83}$	$61.61^{+6.68}_{-6.17}$	$64.51^{+9.46}_{-5.36}$	$63.10^{+41.77}_{-7.48}$	$56.36^{+5.94}_{-5.34}$	$62.32^{+7.33}_{-5.06}$	$58.41^{+8.23}_{-3.38}$	This work
$M_{\star}$ ($M_{\odot}$)	$1.69^{+0.15}_{-0.53}$	$1.41^{+1.45}_{-0.50}$	$1.41^{+0.34}_{-0.35}$	$1.28^{+0.32}_{-0.28}$	$1.76^{+0.31}_{-0.30}$	$1.48^{+0.90}_{-0.38}$	$1.06^{+0.25}_{-0.17}$	$1.46^{+0.31}_{-0.29}$	$0.99^{+0.17}_{-0.13}$	This work
$R_{\star}$ ($R_{\odot}$)	$10.86^{+0.22}_{-0.28}$	$12.49^{+7.97}_{-2.18}$	$11.16^{+0.45}_{-0.38}$	$11.06^{+0.44}_{-0.43}$	$11.21^{+0.66}_{-0.39}$	$11.22^{+3.15}_{-0.45}$	$10.95^{+0.42}_{-0.54}$	$11.22^{+0.55}_{-0.27}$	$11.20^{+0.22}_{-0.24}$	This work
σ_{HIP}	0.011	0.006	0.008	0.006	0.007	0.006	0.005	0.006	0.005	Hipparcos

*As for parallax measurements, superscript "a" refers to Gaia EDR3, and "b" refers to Hipparcos. Takeda08 refers to Takeda, Sato, and Murata (2008), and the subscript "sp" refers to spectral determination.

the H line, respectively. The errors were estimated based on photon noise. If RV variation contained a dominant component of stellar activity, there would be a significant correlation between RV and S_H, e.g., HD 120048 (Sato et al. 2013).

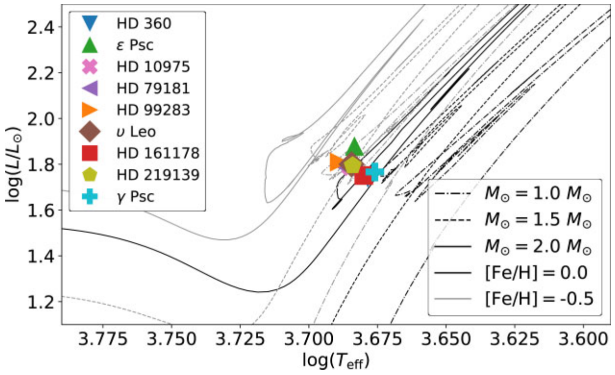

Fig. 1. HR diagram with HD 360, ϵ Psc, HD 10975, HD 79181, HD 99283, υ Leo, HD 161178, HD 219139, and γ Psc. Some evolutionary tracks for masses of 1.0 $M_\odot$, 1.5 $M_\odot$, and 2.0 $M_\odot$ are also shown. The black lines and grey lines correspond to [Fe/H] = 0.0 and [Fe/H] = −0.5, respectively. (Color online)

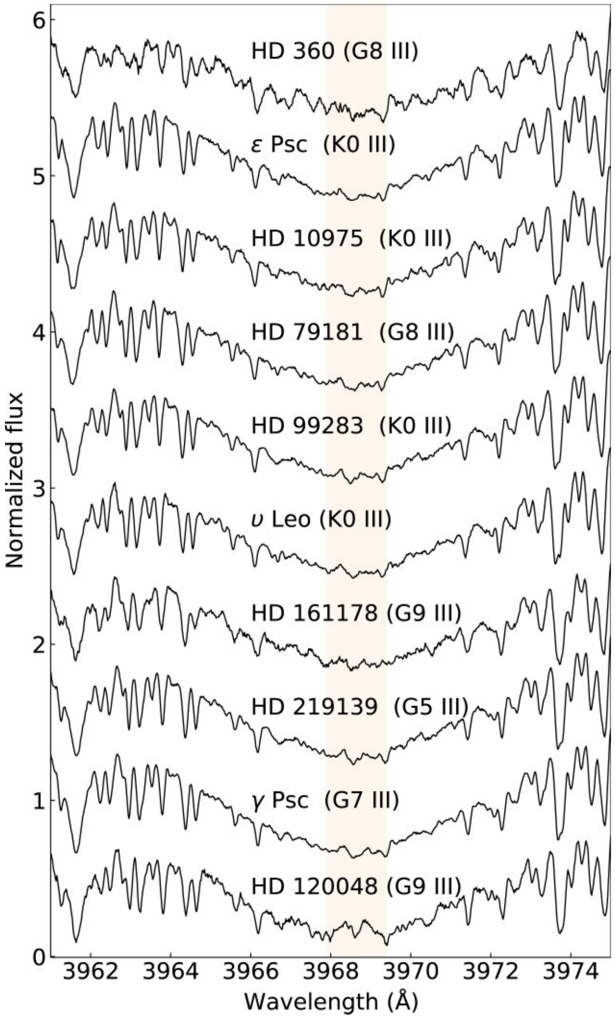

Fig. 2. Spectra in the region of Ca II H lines of HD 360, ϵ Psc, HD 10975, HD 79181, HD 99283, υ Leo, HD 161178, HD 219139, and γ Psc with a comparison of the active star HD 120048. Vertical offsets are added to each normalized spectrum for clarity. (Color online)

4.3 Period search

To search periodicity in the time series, we performed a Generalized Lomb–Scargle (hereafter GLS) periodogram (Zechmeister & Kürster 2009) with `Python` package `astropy`. To assess the significance of the periodicity, we applied False Alarm Probability (FAP) with approximation method developed by Baluev (2008) in the same package. For some stars, to investigate the true period of the candidate further, Stacked Bayesian Generalized Lomb–Scargle periodogram (SBGLS: Mortier & Collier Cameron 2017) was performed so that we could check the evolution of the periods with an increasing amount of data. The main idea of this method is stacking Bayesian GLS periodograms (BGLS:[2] Mortier et al. 2015) from the first n points of data and normalizing periodograms with their respective minimum values. In this way, the power of a signal can be compared over time, and the signal of stable and strong(er/est) power is closer to the true one. The SBGLS has been adopted in similar studies of planet-searching around giant stars, e.g., Tala Pinto et al. (2020).

4.4 Keplerian orbital fit

Orbital motion of planet(s) can account for the stable periodic RV variation of a star. Therefore, Keplerian orbital fitting was performed on each star in order to investigate the validity of the planetary nature. The best-fitting Keplerian orbit for the data was derived by maximum likelihood maximization using Python package SciPy with a truncated Newton (TNC) method and a Nelder–Mead method (Nelder & Mead 1965). The Keplerian model was generated by RadVel (The Radial velocity Modeling Toolkit)[3] (Fulton et al. 2018). The free parameters included Keplerian orbital elements (orbital period P, RV semi-amplitude K, the combination of eccentricity e and argument of periastron ω, $\sqrt{e}\cos\omega$, and $\sqrt{e}\sin\omega$ and time of inferior conjunction $T_{\rm c}$),[4] the RV offset of different instruments $\gamma_{\rm inst}$, and extra Gaussian noise $s_{\rm inst}$. The uncertainties for these

---

[2] BGLS describes the probability that a full sine function with a specific frequency is present in the data, where weights derived from errors on the data and a constant offset is included.

[3] Fulton, B., & Petigura, E. 2017, RadVel: Radial Velocity Fitting Toolkit (doi:10.5281/zenodo.580821).

[4] The pariastron passage $T_{\rm p}$ is converted from inferior conjunction $T_{\rm c}$ after parameter fitting.

Table 2. Priors for MCMC sampling.

Prameter	Prior	Minimum	Maximum	Knee value
P (d)	Jeffrey's	1	10000	—
K (m s^{-1})	Modified Jeffrey's	1.01	100	1
$\sqrt{e}\cos\omega$	Uniform	0	1	—
$\sqrt{e}\sin\omega$	Uniform	0	1	—
$\gamma_{\rm inst}$	Uniform	−200	200	—
$s_{\rm inst}$	Modified Jeffrey's	1.01	100	1

*The subscript "inst" refers to a certain instrument.

parameters were derived by Markov Chain Monte Carlo (MCMC) sampling using `emcee` (Foreman-Mackey et al. 2013). Gelman–Rubin statistics (G–R hereafter; Gelman et al. 2013) were used to check the convergence of the chain during and after burn-in. After the chain first reached the G-R level lower than 1.01, we considered the chain marginally well-mixed and stopped burn-in. After the chain passed five checkpoints of G–R < 1.01 and independent samples T_z (Ford 2006) greater than 1000, we stopped the chain and finished sampling. For the priors, we selected Jeffrey's prior for P, uniform distribution for $\sqrt{e}\cos\omega$, $\sqrt{e}\sin\omega$, and $\gamma_{\rm inst}$, and modified Jeffrey's prior for K and $s_{\rm inst}$. The detailed values for each prior are summarized in table 2. After fitting, we converted the best-fitting values and the uncertainties of $\sqrt{e}\cos\omega$ and $\sqrt{e}\sin\omega$ into e and ω as the final results. To have an evaluation of a long-term trend (liner and quadratic plus linear), which might introduce a possible outer planet, we calculated the reduced chi-square $\chi^2_{\rm red}$ ($\chi^2_{\rm red} = \chi^2/N_{\rm DoF}$, where $N_{\rm DoF}$ is the degree of freedom) and BIC value (Schwarz 1978; BIC $= -2\ln(\hat{L}) + n_{\rm pars}\ln(n_{\rm data})$, where $\hat{L}$ is the maximized value of the likelihood function, $n_{\rm pars}$ is the number of parameters, and $n_{\rm data}$ is the number of data) for models with and without trends. $\chi^2_{\rm red}$ shows the goodness of fits, and the BIC value indicates the difference between models. We ruled out those fittings with $\chi^2_{\rm red}$ far from 1. To determine if we should use a model with a long-term trend, we compared the BIC values of different models. Only if the BIC value of the model with a higher-order trend showed a lower value with a difference greater than 10 (Kass & Raftery 1996) would we take the higher-order trend into further discussion. Finally, we make a comparison against the null hypothesis, which only includes RV jitters and possible linear trends. Here, we also adopt BIC as a criterion. Similarly, only if the Keplerian model had a lower BIC value with a difference greater than 10 did we believe the Keplerian model is significantly better than the null hypothesis.

We also tried to check the consistency in orbital parameters derived from HIDES-S data and HIDES-F ones, respectively. However, for each star, our observations were sparsely distributed over 15 years, especially for those data obtained by HIDES-S. In such a case, we could not perform Keplerian orbital fits by using only HIDES-S data. Thus, we could not clearly know if the best-fitting RV semi-amplitude and orbital period apparently vary in time, which may suggest the possibility of non-planet origin for the observed RV variations. For simplicity, we instead tested the variability of the scattering of original RV data. We divided the data of each instrument into three and calculated the root mean square (rms) of the first, middle, and last third of them for RVs and Julian days (JDs). For HD 360, HD 10975, HD 99283, and γ Psc observed by HIDES-S, we only calculated the rms of all the data due to the small number of their observations (35, 28, 32, and 34 for HD 360, HD 10975, HD 99283, and γ Psc respectively). The rms of JDs were used for illustrating the scatter of observations; in other words, the sparseness of observations. A more constant rms value of RVs could make the Keplerian model more convincing. Concerning solar-like oscillations, poor data sampling, and instrumental drift within a short period of time, the rms values of RVs varying within a few m s^{-1} should be accepted.

5 Results

In this section, we present the solutions of the Keplerian orbits of our nine stars in the Okayama Planet Search Program: HD 360, ϵ Psc, HD 10975, HD 79181, HD 99283, υ Leo, HD 161178, HD 219139, and γ Psc. According to Bayesian analysis, all nine stars favor the one-Keplerian model rather than the null hypothesis. The fitted orbital periods range from 255 to 555 d, and fitted minimum masses range from 0.45 to 1.34 $M_{\rm J}$ with RV semi-amplitude between 11.7 and 34.0 m s^{-1}. With further analyses in RV time series, line profile, and activity indicator, ϵ Psc can only be labeled as a planet-harboring candidate rather than a confirmed planet-harboring star. This is because we found the BIS moderately correlated with RV, and meanwhile, we found BIS varies at similar periods to the RV periodicity. In addition, the possibility that the periodicity varied with time could not be ruled out, thus ϵ Psc was not confirmed as a planet host. As for the other eight stars, they are confirmed to be host planets, and the star HD 360, which showed a strong RV linear trend, is likely to host another outer companion. The orbital parameters of eight planets and one planet candidate are summarized in table 3, and the detailed analysis for each individual star is presented in appendix 3.

6 Discussion

According to Keplerian fitting, planetary orbital motion can be an interpretation of periodic variation in the RV time series of eight G- and K-type giant stars from the Okayama Planet Search Program: HD 360, ϵ Psc,

Table 3. Orbital parameters.*

Parameters	HD 360 b	ϵ Psc b	HD 10975 b	HD 79181 b	HD 99283 b	υ Leo b	HD 161178 b	HD 219139 b	γ Psc b
P (d)	$273.1^{+1.6}_{-0.8}$	$255.3^{+2.1}_{-1.4}$	$283.8^{+12.7}_{-0.1}$	$273.1^{+1.3}_{-0.4}$	$310.4^{+5.2}_{-1.7}$	$385.2^{+2.8}_{-1.3}$	$279.3^{+1.0}_{-0.8}$	$275.5^{+2.3}_{-1.0}$	$555.1^{+6.0}_{-2.5}$
K ($\mathrm{m\,s^{-1}}$)	$16.8^{+1.8}_{-2.6}$	$20.6^{+2.1}_{-2.9}$	$12.3^{+0.2}_{-3.5}$	$17.7^{+1.6}_{-2.2}$	$20.4^{+1.9}_{-3.5}$	$11.7^{+1.7}_{-1.6}$	$17.0^{+1.6}_{-2.3}$	$19.2^{+1.8}_{-2.6}$	$34.0^{+3.9}_{-5.0}$
e	$0.139^{+0.108}_{-0.104}$	$0.278^{+0.122}_{-0.186}$	$0.442^{+0.040}_{-0.389}$	$0.259^{+0.067}_{-0.206}$	$0.200^{+0.102}_{-0.146}$	$0.320^{+0.134}_{-0.218}$	$0.044^{+0.132}_{-0.019}$	$0.110^{+0.087}_{-0.081}$	$0.204^{+0.114}_{-0.141}$
ω (°)	133^{+119}_{-63}	237^{+26}_{-36}	135^{+153}_{-35}	318^{+48}_{-32}	291^{+62}_{-41}	131^{+36}_{-31}	300^{+180}_{-70}	318^{+113}_{-67}	44^{+34}_{-56}
T_{p}(JD−2450000)	$5184.5^{+44.9}_{-92.8}$	$5420.0^{+6.9}_{-85.8}$	$5450.7^{+29.1}_{-182.9}$	$5123.0^{+103.8}_{-11.6}$	$5291.1^{+256.1}_{-25.6}$	$5279.6^{+27.9}_{-34.2}$	$5296.6^{+218.4}_{-12.0}$	$5240.1^{+198.9}_{-12.2}$	$5394.6^{+60.6}_{-63.5}$
$M_{\mathrm{p}}\sin i\,(M_{\mathrm{J}})$	$0.75^{+0.12}_{-0.15}$	$0.77^{+0.16}_{-0.10}$	$0.45^{+0.06}_{-0.15}$	$0.64^{+0.06}_{-0.16}$	$0.97^{+0.06}_{-0.25}$	$0.51^{+0.06}_{-0.26}$	$0.57^{+0.02}_{-0.16}$	$0.78^{+0.05}_{-0.20}$	$1.34^{+0.02}_{-0.31}$
a (au)	$0.98^{+0.11}_{-0.03}$	$0.88^{+0.11}_{-0.10}$	$0.95^{+0.06}_{-0.08}$	$0.90^{+0.07}_{-0.08}$	$1.08^{+0.05}_{-0.07}$	$1.18^{+0.11}_{-0.32}$	$0.85^{+0.05}_{-0.07}$	$0.94^{+0.06}_{-0.07}$	$1.32^{+0.05}_{-0.08}$
s_{s} ($\mathrm{m\,s^{-1}}$)	$16.7^{+4.3}_{-0.7}$	$22.7^{+3.3}_{-1.6}$	$10.2^{+3.0}_{-0.5}$	$14.1^{+2.3}_{-0.5}$	$17.5^{+4.0}_{-1.7}$	$12.5^{+2.6}_{-0.7}$	$15.9^{+2.1}_{-0.8}$	$16.6^{+3.3}_{-1.0}$	$27.7^{+6.5}_{-2.1}$
s_{f} ($\mathrm{m\,s^{-1}}$)	$12.3^{+1.9}_{-0.7}$	$14.5^{+2.1}_{-0.5}$	$9.6^{+1.6}_{-0.5}$	$14.7^{+1.7}_{-1.2}$	$11.3^{+2.5}_{-0.4}$	$8.4^{+1.5}_{-0.4}$	$14.8^{+1.9}_{-0.8}$	$12.5^{+2.0}_{-0.6}$	$21.0^{+4.2}_{-1.1}$
γ_{s} ($\mathrm{m\,s^{-1}}$)	$11.6^{+3.0}_{-3.7}$	$-2.2^{+3.6}_{-2.8}$	$-0.5^{+2.2}_{-2.4}$	$0.1^{+1.7}_{-1.7}$	$-0.3^{+3.5}_{-4.1}$	$1.2^{+1.8}_{-2.5}$	$2.7^{+2.0}_{-2.1}$	$1.1^{+2.5}_{-3.4}$	$0.5^{+4.0}_{-5.2}$
γ_{f} ($\mathrm{m\,s^{-1}}$)	$-27.9^{+3.8}_{-3.4}$	$0.7^{+1.8}_{-1.7}$	$1.1^{+1.0}_{-1.7}$	$0.4^{+2.0}_{-1.7}$	$-0.1^{+1.9}_{-1.7}$	$-1.2^{+1.3}_{-1.6}$	$-0.4^{+1.8}_{-1.8}$	$-4.9^{+2.0}_{-1.5}$	$-2.5^{+3.6}_{-3.2}$
$\dot{\gamma}$ ($\mathrm{m\,s^{-1}\,d^{-1}}$)	$0.018^{+0.002}_{-0.002}$	—	—	—	—	—	—	—	—
$\ddot{\gamma}$ ($\mathrm{m\,s^{-1}\,d^{-2}}$)	—	—	—	—	—	—	—	—	—
rms ($\mathrm{m\,s^{-1}}$)	14.8	18.9	10.7	15.5	14.4	11.2	16.0	15.1	24.6
χ^2_{red}	1.142	1.083	1.119	1.075	1.143	1.115	1.072	1.107	1.140
BIC	885.5	1295.4	793.5	1420.6	712.4	848.1	1346.1	967.1	868.5
ΔBIC	−25.0	−32.7	−10.0	−46.5	−19.2	−22.3	−33.5	−30.2	−26.2
$N_{\mathrm{obs,\,s}}$	35	60	31	92	28	46	77	42	35
$N_{\mathrm{obs,\,f}}$	67	84	67	72	54	59	77	69	54
t_{start} (Year/month)	2004/01	2002/02	2004/01	2001/03	2004/01	2001/12	2001/03	2004/01	2002/02
t_{end} (Year/month)	2017/12	2017/11	2017/12	2017/12	2017/11	2017/11	2017/12	2017/12	2017/12
Detection	Planet	Candidate	Planet	Planet	Planet	Planet	Planet	Planet	Planet

*The subscripts “s” and “f” refer to results related to HIDES-S data and HIDES-F data, respectively. ΔBIC is defined as $\Delta\mathrm{BIC} = \mathrm{BIC} - \mathrm{BIC}_0$, where BIC_0 is the BIC value of null hypothesis.

HD 10975, HD 79181, HD 99283, υ Leo, HD 161178, HD 219139, and γ Psc. With further analysis in RV time series, line profiles, and stellar activity indicator, however, it is indicated that the RV variation of ϵ Psc might intrinsically be from the star itself. Therefore we only label ϵ Psc as a planet-harboring candidate. In the planetary explanation, nine planetary companions including the candidate orbit their host stars with semimajor axes around 1 au, and seven of the nine have the lowest minimum masses ever discovered around solar-mass to intermediate-mass giant stars. Interestingly, RV variations of five stars (HD 360, HD 10975, HD 79181, HD 161178, HD 219139) have similar RV variability around 280 d. Is this a coincidence? In the subsequent part of this section, we first put forward another two alternative scenarios to explain the regular RV variation. Then, we discuss eccentricities and detectability of planets around G- and K-type giant stars. Finally, we discuss the metallicity of planet-harboring intermediate-mass stars.

6.1 Stellar rotation of G- and K-type giant stars

From the Lick survey, Saar et al. (1998) proposed the relationship between rotational velocity with stellar jitter among dwarf stars. However, we know less about G- and K-type giant stars regarding their rotations, since these stars are usually very slow rotators with rotating periods of a few hundred days. Strong activity such as starspots accompanying rotation could probably cause RV variation similar to the Keplerian RV variation. For the nine stars in this work, we did not find significant periodicity from the Hipparcos photometry and Ca II H index S_{H}, where we could not recognize their stellar rotation periods. Therefore, at least for the nine stars in this work, there is little evidence that activity accompanied with stellar rotation is the source of regular RV variations, yet the lack of decade-long chromatic RV measurements and photometry means that activity-related variability could not fully be discarded. Furthermore, we collect known planet-harboring G- and K-type giant stars showing RV semi-amplitude less than $50\,\mathrm{m\,s^{-1}}$, and compare the expected rotational periods with their planet orbiting periods. Since the stellar rotations are given in projected velocities $v \sin i$, we therefore take the mean value of $\sin i \simeq 0.637$ and converted velocities into days.[5] As seen in figure 3, most of the reported planets including the nine ones in this research (under planetary nature) have orbital periods longer than the expected stellar rotation periods. We also see that the expected rotation periods concentrate around 200–300 d, while there is no concentration in the histogram of the orbital period. We calculated Pearson's correlation coefficient for these data, and it returns $r = 0.08$, suggesting a weak correlation. Statistically, this implies that the similar RV variations in G- and K-type giant stars are not related to stellar rotation, while we doubt a small number of individuals might refer to it.

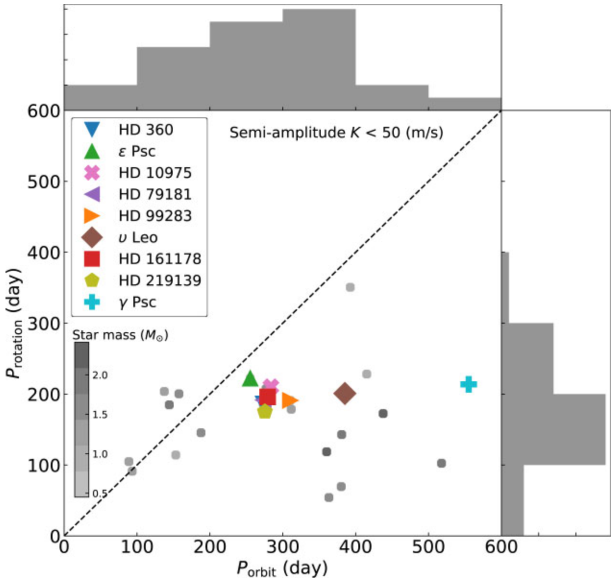

Fig. 3. Stellar rotational against planetary orbital period. Filled dots are G- and K-type planet-hosting giant stars with their planets showing RV semi-amplitude weaker than $50\,\mathrm{m\,s^{-1}}$. (Data were collected on 2019 May 30.) (Color online)

6.2 Long secondary periods in giant stars

Long secondary periods (LSP) is a mysterious phenomenon that happens to some very high luminosity (usually $L > 300\,L_{\odot}$ Saio et al. 2015) giant stars. Typically, this LSP ranges from about 200 d to 1500 d and co-exists with a primary period which is eight times shorter. Observations showed RV variation of a few $\mathrm{km\,s^{-1}}$ (Wood et al. 2004; Nicholls et al. 2009) and photometry variation of up to 1 mag (Saio et al. 2015), and periods in both patterns consist well with each other. Hatzes et al. (2018) showed a new form of stellar variability in the K-type giant star γ Dra (K5 III, $B - V = 1.53$), and Reichert et al. (2019) showed similar variation in another K-type giant star, Aldebaran (K5 III). The true mechanism of LSP is not yet fully understood. Saio et al. (2015) proposed that LSP could relate to oscillatory convective modes in red giants. The variability in these two stars is also possibly related to oscillatory convective modes and behaves similarly to planetary signals in RV, showing an RV semi-amplitude over $100\,\mathrm{m\,s^{-1}}$. Döllinger and Hartmann (2021) also raised the feasibility that oscillations and other phenomena could mimic exoplanets, especially for stars larger than $21\,R_{\odot}$. Compared to K-type giant stars, the RV variations of which are usually up to several hundred $\mathrm{m\,s^{-1}}$, our late-G and early-K giant stars with $0.8 < B - V < 1.0$ and $R \sim 10\,R_{\odot}$ in this research have better intrinsic stability in RV at a level of $\sigma \sim 20\,\mathrm{m\,s^{-1}}$ (Henry et al. 2000; Sato et al. 2005). Soszyński et al. (2021) proposed the binarity origin of LSP by characterization of the near-infrared light curves, which illustrates that the nature for the LSP modulation is obscured by a dusty cloud orbiting the red giant star with a substellar or stellar companion. In this scenario, the companion originates from a planet and accretes a huge amount of mass from the envelope of its host star. If so, we could assume that our targets are precursors of substellar or stellar companions, which does not negate the planet explanation of RV variations of our stars in this study.

---

[5] The average of $\sin i$ is $\overline{\sin i} = (1/\pi)\int_0^{\pi} \sin i\, di \simeq 0.637$.

Nonetheless, in recent research, Heeren et al. (2021) showed additional regular variations with a period of 291 d in the spectroscopic binary ϵ Cyg. We notice this period is close to our detection of near 300 d periods. Importantly, the main star ϵ Cyg A (K0 III, 1.1 $M_{\odot}$) shows similar stellar properties (Heeren et al. 2021) to our targets. In their work, Heeren et al. (2021) ruled out planetary hypothesis by detection of apparently time-varying RV amplitude and orbital period, and failure in orbital stability analysis. Although it was proposed that the 291 d regular variation of ϵ Cyg A seemed to be a possibly extreme example of a heartbeat system, they did not fully exclude the mechanism of LSP. Combining stars in Heeren et al. (2021) and this work, they all share similar stellar properties and periodic RV variation. So, here we may leave a question: do they originate from the same intrinsic variation of stars? We should take notice of one essential difference, that eight of our nine stars are single stars. Although ϵ Psc is a suspected double star with separation around 1000 au ($0.''03$; Mason et al. 2001), the separation is more than 60 times wider than Cyg A and B, for which we do not consider the heartbeat. Thus, the most likely heartbeat scenario for the ϵ Cyg system can be easily rejected to our stars. Since Heeren et al. (2021) did not fully eliminate the possibility of LSP, it is reasonable to suspect they are all of LSP origin.

In other words, even if the stellar properties of our stars do not comform well with the currently known LSP star, due to the probably incomplete knowledge of LSP, we could not fully rule out the LSP explanation. Furthermore, our nine stars in this work share similar stellar properties. As we can see in the HR diagram (figure 1), all nine stars concentrate around $\log(T_{\rm eff}) \simeq 3.68$ and $\log(L/L_{\odot}) \simeq 1.8$. We infer that this is most likely to be the result of target screening of the Okayama Planet Search Program (Sato et al. 2005). Yet, due to similarities in stellar properties, we still reserve the explanation that the nearly 280 d periodic variation might relate to another new form of intrinsic stellar variability of G- and K-type giant stars.

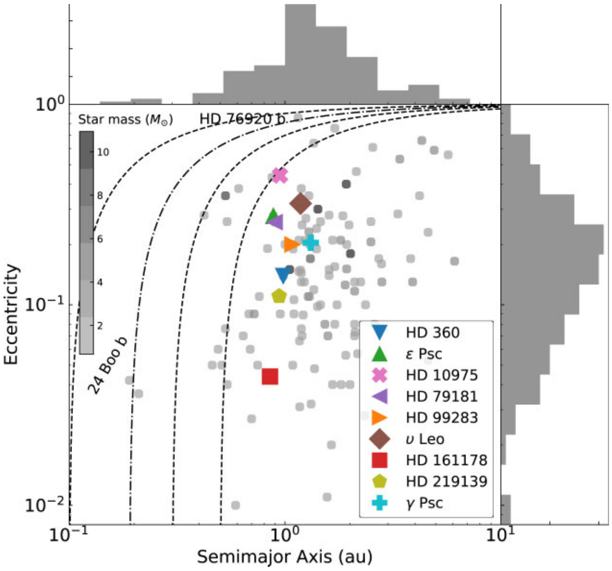

Fig. 4. Eccentricity as a function of semimajor axis. Filled circles are planets around G- and K-type giant stars, with their darkness representing the mass of their host stars. The dash–dotted curve represents periastron distance $q = 0.2$ au, and dashed curves represent periastron distance q equal to 0.1, 0.3, and 0.5 au from left to right, respectively. The periastron distance is $q = a(1 - e)$, where a is the semimajor axis and e is eccentricity. All axes and histograms are in logarithm. (Data were collected on 2019 May 30.) (Color online)

6.3 Eccentricity of planets around G- and K-type giant stars

According to Keplerian fitting results, HD 161178 b ($e = 0.044$) orbits its hosts in near circular ($e < 0.1$) orbits, while HD 360 b ($e = 0.139$), the candidate ϵ Psc b ($e = 0.278$), HD 10975 b ($e = 0.442$), HD 79181 b ($e = 0.264$), HD 99283 b ($e = 0.198$), υ Leo b ($e = 0.320$), HD 219139 b ($e = 0.110$), and γ Psc b ($e = 0.204$) orbit their hosts in possible eccentric orbits. HD 10975 b refers to a rare case among current observations, having a best-fitting eccentricity that exceeds 0.4. Besides, this planet is the least-massive giant planet ever found around a giant star and it has the shortest orbital period among highly eccentric planets around giant stars. Figure 4 shows eccentricity as a function of the semimajor axis. Among planets found orbiting intermediate-mass and solar-mass evolved stars, 38% were found with eccentricity lower than 0.1, and 85% were found with eccentricity lower than 0.3. Eccentricity in logarithm shows that orbits of giant planets around G- and K-type giant stars are seldom extremely circular, and 72% are found between 0.045 and 0.25. Additionally, we adopted a Kolmogorov–Smirnov (K–S) test (Kolmogorov 1933; Smirnov 1948) on eccentricities of planets around solar-mass and intermediate-mass evolved stars against the main sequence stars. The test showed a probability of 0, which convinces us that they are apparently different distributions. Besides, we found that only three planets: 24 Boo b

(Takarada et al. 2018), HD 76920 b (Wittenmyer et al. 2017b), and Kepler-91 (Lillo-Box et al. 2014; Sato et al. 2015) were found residing within the periastron distance of 0.2 au, where it includes the most eccentric planet orbiting an evolved star.

Several scenarios are proposed to explain the origin of the high eccentricities of the exoplanets. One of them is the Kozai–Lidov mechanism (Kozai 1962; Lidov 1962), in which a planet can be driven from a nearly circular orbit to a highly eccentric orbit due to an inclined, external perturber such as a stellar companion or an outer planetary companion. This seems to be the scenario of two well-known extremely eccentric planets: HD 20782 b (Jones et al. 2006; Udry et al. 2019) and HD 80606 b (Wittenmyer et al. 2007; Stassun et al. 2017), the systems of which contain stellar companions. Since no stellar companion was found around HD 10975 b, yet no RV trend suggesting the existence of outer bodies was found in the residuals, the Kozai–Lidov mechanism should not be the true scenario for this star.

Planet–planet scattering is another possible explanation. We assume that HD 10975 b has been scattered into the current highly-eccentric orbit by another unobserved planet in the system. If so, there should be another signal in the star's RV time series. Yet, except for the signal of HD 10975 b, we did not find any long-term trend or any periodicity in the RV residuals, which means this hypothetical planet does not appear near the HD 10975 system "at this moment." In this case, we reserve the scenario that an outer body was ejected out of the system "a long time ago." Then, we assume that the unobserved planet has been ejected away from the system, or it has been scattered into an inner orbit and soon engulfed by its host. BD +48 740, a lithium-rich star, is supposed to be the case that the existence of a highly eccentric planet was caused by planet–planet scattering, and consequently, one planetary companion was engulfed by its host star (Adamów et al. 2012, 2018). However, by measuring the lithium abundance of HD 10975 (Liu et al. 2014), we found an upper limit of $A(\mathrm{Li}) \leq 0.35$; no lithium overabundance has happened compared with other giant stars. This suggests that probably there is not a planet scattered into the host star due to the interaction with HD 10975 b. In brief, although we did not find any evidence, planet–planet scattering is a satisfactory explanation.

6.4 Detectability of less-massive planets around G- and K-type giant stars

Among our nine targets, HD 360 b ($M_\mathrm{p}\sin i = 0.75\,M_\mathrm{J}$, $a = 0.98$ au), the candidate ϵ Psc b ($M_\mathrm{p}\sin i = 0.77\,M_\mathrm{J}$, $a = 0.87$ au), HD 10975 b ($M_\mathrm{p}\sin i = 0.45\,M_\mathrm{J}$, $a = 0.95$ au), HD 79181 b ($M_\mathrm{p}\sin i = 0.64\,M_\mathrm{J}$, $a = 0.90$ au), υ Leo b ($M_\mathrm{p}\sin i = 0.51\,M_\mathrm{J}$, $a = 1.18$ au), HD 161178 b ($M_\mathrm{p}\sin i = 0.57\,M_\mathrm{J}$, $a = 0.85$ au), and HD 79181 b ($M_\mathrm{p}\sin i = 0.78\,M_\mathrm{J}$, $a = 0.94$ au) are the least massive planets ($M_\mathrm{p}\sin i \lesssim 0.9 M_\mathrm{J}$) ever discovered around G- and K-type giant stars, including those of both intermediate-mass (1.5–5 $M_\odot$) and solar-mass (0.7–1.5 $M_\odot$). Before this research, only planetary companions more massive than 0.9 M_J were detected around the G- and K-type giant stars: BD +48 738 b ($M_\mathrm{p}\sin i = 0.91\,M_\mathrm{J}$; Gettel et al. 2012) and 24 Boo b ($M_\mathrm{p}\sin i = 0.91\,M_\mathrm{J}$; Takarada et al. 2018). Here we did not take transit detected Kepler-91 (Lillo-Box et al. 2014; Sato et al. 2015) into account.

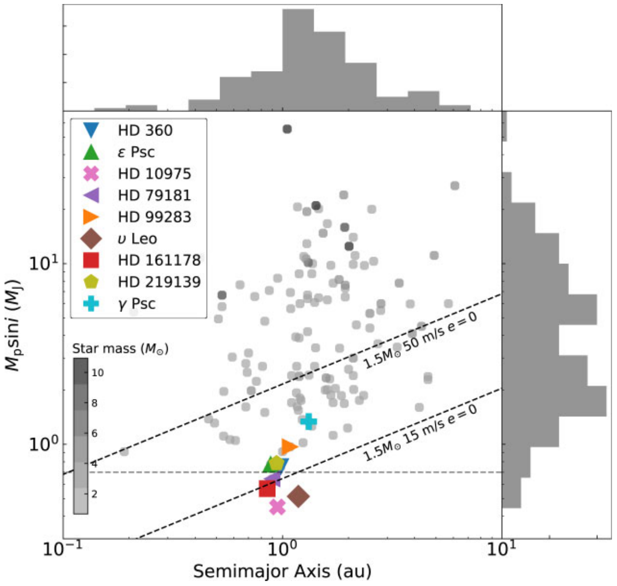

Fig. 5. Minimum mass of planet as a function of semimajor axis. Filled circles are planets around G- and K-type giant stars, with their darkness representing the mass of their host stars. The horizontal dashed line represents the minimum mass of 0.7M_J. Two sloped dashed lines show, respectively, detectabilities of planets around their host stars generating RV semi-amplitude of 15 m s^{-1} and 50 m s^{-1} in circular orbits. (Data were collected on 2019 May 30). (Color online)

Figure 5 shows the minimum mass as a function of semimajor axis. As is shown in the figure, almost no planet exceeded the detectability of a planet circularly orbiting a star of 1.5 $M_\odot$ with a radial velocity semi-amplitude of 15 m s^{-1}. Pushing the detection limit to a lower level will allow us to make a direct comparison of mass distribution among giant exoplanets between a wider range of distance to the host stars and the mass of their host stars.

Normally, it is difficult to detect planets with $\lesssim 2\,M_\mathrm{J}$ around G- and K-type giant stars via Doppler measurements because the stellar oscillation raises the RV variation to a level of 10–20 m s^{-1}, which means RV signals below 30 m s^{-1} could be hard to recognize or detect (Jones et al. 2014). We evaluated the RV jitters induced by stellar oscillation in this work. By using the empirical functions in Yu et al. (2018) and stellar parameters determined in this work, all nine stars have RV amplitudes around or lower than a level of $\sim 10\,\mathrm{m\,s^{-1}}$. At the same time, they should also be lower than the rms of their residuals. Sato et al. (2013) studied the features of RV variations in the G- and K-type giant stars by high cadence observations, showing that solar-like oscillations dominate in these variations with periods of 3–10 hr. However, unlike dwarf stars, the p-mode (acoustic pressure mode) oscillation period of which is around 10 min, the p-mode oscillation of giant stars is difficult to average out with longer integration times (e.g., Mayor & Udry 2008; Dumusque et al. 2011).

Thus in this study, we further generated simulations in order to explore the detectability of giant planets with various minimum masses around different stars. For each planet mass around each star mass, we generated over 378000 independent RV curves, yet some other conditions, i.e., orbital period, and instrumental and stellar jitter, are different. For the sake of simplicity, we only injected random instrumental RV shifts and RV variation caused by solar-like oscillations to the Keplerian RV curve. In each simulation, the instrumental RV shifts were set to be a uniformly distributed random value. The maximum of the instrumental RV shifts in each simulation is also randomly determined with a uniform distribution between 2 and $6\,\mathrm{m\,s^{-1}}$. We did not adopt Gaussian noise in instrumental RV shifts here, since we have no evidence that the long-term HIDES instrumental RV shift was Gaussian-like according to the instrumental RV stability analysis in section 4. The jitter caused by solar-like oscillations was set to be Gaussian with boundaries at 3σ. Empirically, the jitter caused by solar-like oscillations of a G- or K-type giant star is approximately a few to $20\,\mathrm{m\,s^{-1}}$. We thus set the error of the Gaussian to be a uniformly distributed random number between 6 and $18\,\mathrm{m\,s^{-1}}$ for each simulation. In a single RV curve, we carried out two simulations with time baselines of 10 years (80 data points) and 15 years (120 data points). All input values in the simulations were set empirically according to frequently observed stars in the Okayama Planet Search Program. In addition, data points were almost uniformly distributed along the time baseline, and there was at most one observation in each week. As they were quantified with the K–S test (Kolmogorov 1933; Smirnov 1948), we knew our simulated observations were more uniformly distributed than real HIDES observations along the baseline. In the simulations, successful recognition of the planet was defined as the case where the strongest signal in GLS indicated the orbital period within an accuracy of 5% and with a FAP value lower than 0.01%.

The simulation results are shown in figure 6. From the figure, it is clear that a planet with minimum mass $2.0 M_\mathrm{J}$ could be easily detected around a star with $2.0\,M_\odot$ with an orbital period over 1000 d. In contrast, a planet with a minimum mass of $0.5\,M_\mathrm{J}$ orbiting a star with $1.5\,M_\odot$ at 300 d with 15-year observations has a successful detection probability lower than 0.7. Generally, when the minimum planet mass is higher than $1\,M_\mathrm{J}$, it maintains a high successful detection ratio for an orbital period of a few hundred days. Yet, as the minimum planet mass becomes lower than $1 M_\mathrm{J}$, the successful detection ratio sharply decreases. The simulation also legibly tells us that planets with shorter orbital periods are much easier to detect. A planet with a minimum mass of $0.8\,M_\mathrm{J}$ orbiting around a star of $1.5\,M_\odot$ at the orbital period of 800 d only has a successful detection possibility of 0.6 and 0.8 with 10 year and 15 year observational baselines, respectively. Here we highlight that, for each simulation, the observational dates are more uniformly distributed than the true HIDES observations along the observational baseline, and on average there are more observations on each star. Furthermore, the simulation illustrates that a hypothetical giant planet in the so-called "planet desert" can be easily detected. Even if a planet has a minimum mass of $0.5\,M_\mathrm{J}$ and is orbiting a star with $1.5\,M_\odot$, it can be detected with a probability higher than 0.8 for a 15 year observation. As introduced in section 1, different surveys have targeted thousands of G- and K-type giant stars for many years, yet only few giant planets are detected inside "planet desert," the boundary of which is around 0.5 au, referring to the orbital period of 100–200 d. This implies that the desert of giant planets around

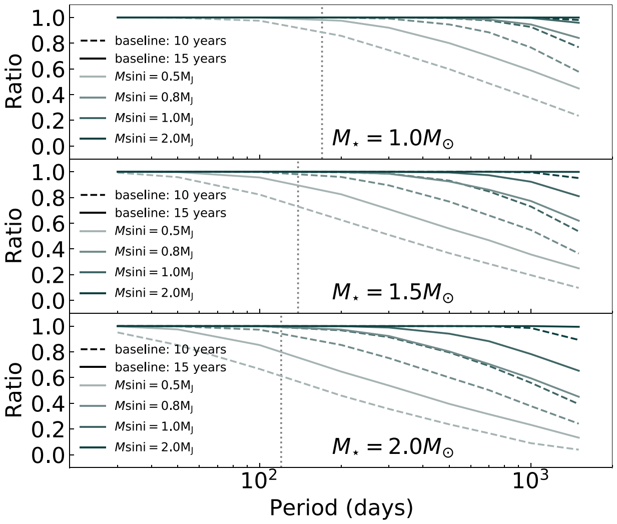

Fig. 6. Ratio of successful detection against simulated orbital periods. From the top to bottom panels, we simulated stars of $1.0\,M_\odot$, $1.5\,M_\odot$, and $2.0\,M_\odot$, respectively. In each panel, planets with minimum masses of $0.5\,M_\mathrm{J}$, $0.8 M_\mathrm{J}$, $1.0 M_\mathrm{J}$, and $2.0 M_\mathrm{J}$ are shown from light-colored lines to dark-colored lines respectively, and observational baselines of 10 years and 15 years are respectively given in dashed curves and solid curves. The vertical dotted line in each figure refers to 0.6 au, the area inside which we name "planet desert". (Color online)

giant stars is likely to be true. Therefore, in terms of successful detection probability, we consider it is rational that less-massive planets ($M\sin i \lesssim 1M_{\rm J}$) just beyond the "planet desert" can be more easily detected, whereas those in wider orbits are not.

As for other studies, Medina et al. (2018) tested simulated p-mode oscillation on subgiant stars, which have p-mode oscillation periods slightly shorter than that of giant stars and RV variations of around 5–10 $\mathrm{m\,s^{-1}}$, and they presented possible techniques to detect Neptunian-mass planets around subgiant stars. To handle the correlated noise of the star, an efficient method could be Gaussian Process (GP) regression. Different studies (e.g., Grunblatt et al. 2016, 2017; Foreman-Mackey et al. 2017; Farr et al. 2018) have shown that planets hidden under noise signals, such as oscillation, granulation, or rotation, can be regressed with a Keplerian or transit plus a GP model.

Several missions, e.g., Transiting Exoplanet Survey Satellite (TESS) and CHaracterising ExOPlanet Satellite (CHEOPS) , are currently ongoing and are opening up a new world of exoplanets. Predicted by Barclay, Pepper, and Quintana (2018), 25% of the total ~300 close-in ($P < 85$ d) planets with radii $R > 4\,R_{\oplus}$ will be detected around evolved intermediate-mass stars in the TESS survey. RV follow-ups to these stars with mitigated stellar jitter should provide us more information about planets around these evolved intermediate-mass stars. Even for those non-transiting targets, high cadence photometric observations given by TESS will provide us information on asteroseismology and stellar rotation, which will probably help us handle noise in the future RV survey.

6.5 Metallicity of planet-harboring intermediate-mass stars

When discussing the occurrence rate of giant planets, many studies showed that they tend to occur around more metal-rich stars, including main sequence stars (e.g., Fischer & Valenti 2005), and giant stars (e.g., Reffert et al. 2015). In this research, we mainly focus on the metallicity distribution of intermediate-mass planet-harbouring stars. Figure 7 shows a mass or minimum mass of currently known planets around intermediate-mass stars against the metallicity of these stars. Here we give our discussion under the planetary explanation of the regular RV variations. According to the mass estimation of the prospective planets in this work and the metallicity of their host stars, the nine systems in this work are all located at the lowermost left-hand region in this figure. We note that the nine stars are all metal-poor stars, having an average metallicity of −0.25 dex, with the richest one of −0.06 dex and the poorest one of −0.62 dex. At present, the most metal-poor planet-harboring intermediate-mass star is BD +20 2457 ([Fe/H] = −1.00; Niedzielski et al. 2009), a K-type giant star that has two substellar companions.

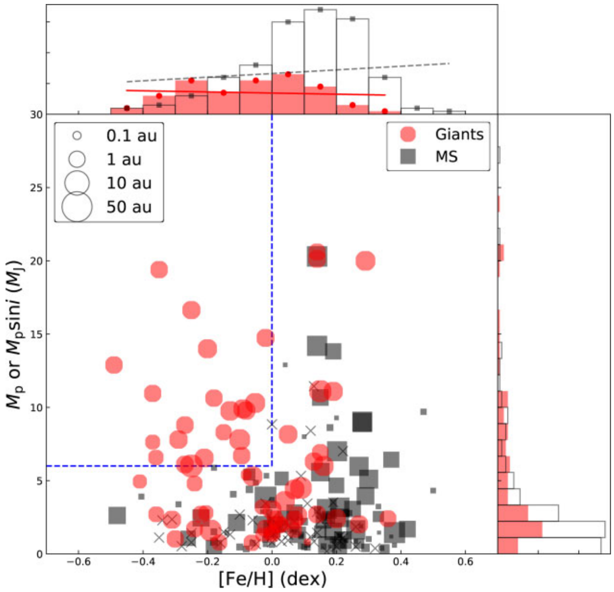

Fig. 7. Mass or minimum mass of giant planets versus metallicity of their host stars, with the size of the dots indicating the orbital semimajor axis of the planet. All dots are intermediate-mass planets harboring stars; red circular ones represent giant stars, grey squared ones represent main-sequence stars, and grey crosses represent main-sequence stars without measurements of orbital semimajor axes of their planets. For both histograms, solid red bars show the counts of giant stars, while the black-framed white bars show the counts of main-sequence stars. In particular, in the horizontal histogram, the solid red line and the black dashed line show the trends of the histograms of giant stars and main-sequence stars, respectively. In addition, and only in this figure, we simply define giant stars as those which have stellar radii greater than five solar radii. (Data were collected at the end of 2019). (Color online)

In the horizontal histogram of figure 7, it is not hard to find a clear increasing trend for the number of detected giant planets around main-sequence stars with the metallicity of their host stars, especially between the range of [Fe/H] = −0.5 and [Fe/H] = 0.3. In contrast, the distribution seems more uniform for detected giant planets around giant stars, especially in the region between [Fe/H] = −0.4 and [Fe/H] = 0.2. Although the number of detections and the occurrence rate does not mean the same thing, the total detected number does not seem to be as little as it is thought to be. When considering only the number of detections, the number of planets around metal-poor stars ([Fe/H] < 0) is slightly larger than the number of those around metal-rich stars ([Fe/H] > 0). In addition, in the area of [Fe/H] < 0 and $M_{\rm p}$ or $M_{\rm p}\sin i > 6\,M_{\rm J}$ (upper left-hand region bound by dashed blue lines), there are almost only giant planets around giant stars at relatively wide orbits ($\gtrsim$1 au), and the giant planets in this area contribute nearly half of those around metal-poor giant stars. We notice that our discussion reaches an agreement with recent research given by

Santos et al. (2017). They indicated that, on average, the metallicity of stars with more-massive giant planets ($4 M_\mathrm{J}$) is lower than the metallicity of those with less-massive giant planets (see the definition in section 3 of that reference), and this is especially so for stars more massive than $1.5\,M_\odot$.

In the current exploration of giant exoplanets around giant stars, statistically, the minimum mass peaks at around $1.5\,M_\mathrm{J}$ and few planets were found within a mass range greater than $3\,M_\mathrm{J}$ and less than $6\,M_\mathrm{J}$, as shown by both figures 5 and 7. This gap is close to the distinction between Jupiter-like planets and substellar companions. Moreover, when the distribution is given in logarithm rather than linearly, the valley at around $3.5\,M_\mathrm{J}$ can be more clearly found. This shows a good agreement with the valley, of $4\,M_\mathrm{J}$, found by Santos et al. (2017) around whole "solar-type" stars. Santos et al. (2017) proposed the boundary as the distinction of two populations of giant planets, and giant planets on both sides originate from different mechanisms—lighter ones are formed via core-accretion while heavier ones are formed via disk instability—and it could be an explanation for the abundant, more-massive giant planets around metal-poor stars. Narang et al. (2018) studied candidates at relatively short orbits around M4 to F0 type main-sequence stars in Kepler DR25 and confirmed this $4\,M_\mathrm{J}$ boundary.

However, when only taking intermediate-mass main-sequence stars into account, the valley does not seem to exist in figure 7. Here, one possible explanation could be inadequate sampling. Compared to over 800 solar-type giant planet hosts given in Santos et al. (2017), around 120 intermediate-mass main-sequence stars represents a minority, which may not correctly reflect the true regimes in mass distribution. Nonetheless, we can boldly infer that the $\sim 4\,M_\mathrm{J}$ valley could be a clue to further investigate planet formation theories. Likewise, it is hard to explain the lack of massive giant planets orbiting metal-poor main-sequence stars in the upper left-hand region in figure 7. As these planets are all orbiting stars in their evolved stage, they should have survived when their host stars evolved out of the main-sequence stage. The absence of massive giant planets around metal-poor intermediate-mass stars in their main-sequence stage suggests inadequate sampling could be the best explanation. In the future, it is necessary to enlarge the samples via different detection methods. Space missions, e.g., TESS and CHEOPS, will also offer us new observations to examine today's conjectures.

6.6 Summary

In this research, we have successfully detected regular RV variations in nine G- and K-type giant stars from the Okayama Planet Search Program: HD 360, ϵ Psc, HD 10975, HD 79181, HD 99283, υ Leo, HD 161178, HD 219139, and HD 219615. Eight of them are best explained as planets, while ϵ Psc is classified as a candidate. The planets will probably end in the engulfment as the stars evolve with time. Among the nine hypothetical planets, HD 360 b is probably accompanied by an outer body, indicated by the linear RV long-term trend, and HD 10975 b is a candidate of highly eccentric planets, although we are not confident about its mechanism. In addition, seven of the nine planets (including one candidate) are the least massive planets ($M_\mathrm{p} \sin i \lesssim 0.9 M_\mathrm{J}$) discovered around evolved giant stars, which pushes down the detectability of planets around giant stars with RV method. In addition, these nine giant stars are all metal-poor stars. By further investigating the metallicity, we confirmed the abundant, more-massive giant planets around metal-poor stars and the mass valley around $4\,M_\mathrm{J}$, which could be interpreted as the distinct boundary of different giant planet formation mechanisms. As a coincidence of variability appears at around 280 d among five stars, we do not fully reject that some of the periodic RV variations intrinsically come from stars themselves, e.g., LSP or another new type of stellar variation.

Supplementary data

The following supplementary data is available at *PASJ* online.

A complete data listing including RV, FWHM, BIS, and S/N for tables 4–12.

Acknowledgment

This research is based on data collected at the Okayama Astrophysical Observatory (OAO), which is operated by the National Astronomical Observatory of Japan. We are grateful to all the staff members of OAO for their support during the observations. Data of τ Cet and ϵ Vir were partially obtained during an engineering time at OAO. We thank the observatory for allowing us to use the data obtained during that time. We thank students of Tokyo Institute of Technology and Kobe University for their kind help with the observations at OAO. B.S. was partially supported by MEXT's program "Promotion of Environmental Improvement for Independence of Young Researchers" under the Special Coordination Funds for Promoting Science and Technology, and by Grant-in-Aid for Young Scientists (B) 17740106 and 20740101 and Grant-in-Aid for Scientific Research (C) 23540263 from the Japan Society for the Promotion of Science (JSPS). H.I. is supported by Grant-in-Aid for Scientific Research (A) 23244038 from JSPS. This research has made use of the SIMBAD database, operated at CDS, Strasbourg, France. This work has made use of data from the European Space Agency (ESA) mission Gaia (https://www.cosmos.esa.int/gaia), processed by the Gaia Data Processing and Analysis Consortium (DPAC, https://www.cosmos.esa.int/web/gaia/dpac/consortium). Funding for the DPAC has been provided by national institutions, in particular the institutions participating in the {Gaia} Multilateral Agreement. This research has made use of the NASA Exoplanet

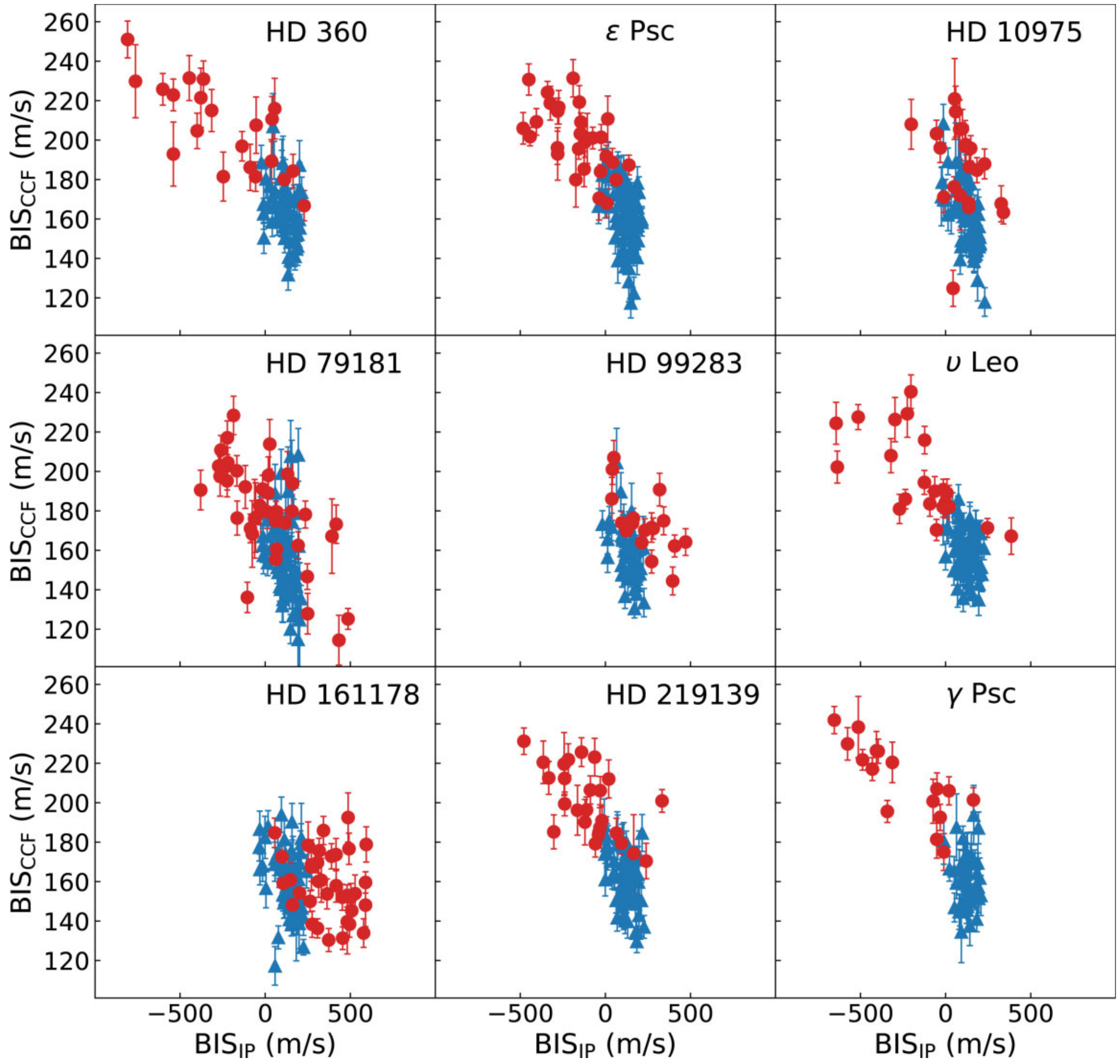

Fig. 8. Relation between $\mathrm{BIS_{CCF}}$ and $\mathrm{BIS_{IP}}$. Red points are obtained from HIDES-S and blue points are obtained from HIDES-F. (Color online)

Archive, which is operated by the California Institute of Technology, under contract with the National Aeronautics and Space Administration under the Exoplanet Exploration Program.

Appendix 1. Effect of IP variability on line profile analysis

The spectral line deformation can be caused by either instrumental variation or stellar surface modulation. The rotational velocities of stars in this work are comparable to or lower than the velocity resolution of HIDES, therefore the BIS of CCF ($\mathrm{BIS_{CCF}}$) might be affected by IP variations. In such a case, we examine the BIS of the mean IP ($\mathrm{BIS_{CCF}}$) which is derived from RV analysis. The IP is estimated within a different wavelength region as bisector analysis; still, we can expect they share the same variability. To calculate $\mathrm{BIS_{CCF}}$, we convert pixels to wavelength in each segment, as IP is described as a function of pixels. The center

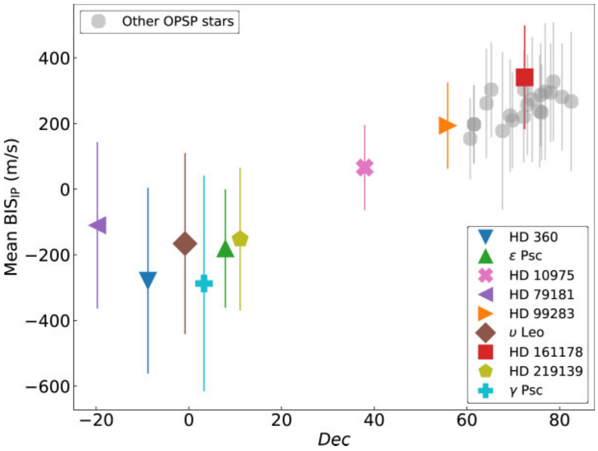

Fig. 9. Mean $\mathrm{BIS_{IP}}$ measured from slit mode spectra against stars' declination. In the figure, the colored dots in different shapes refer to nine stars in this study, and the circular grey dots refer to other stars with Dec $>+60^{\circ}$ in the Okayama Planet Search Program. The error bars indicate the rms scatters of $\mathrm{BIS_{IP}}$. (Color online)

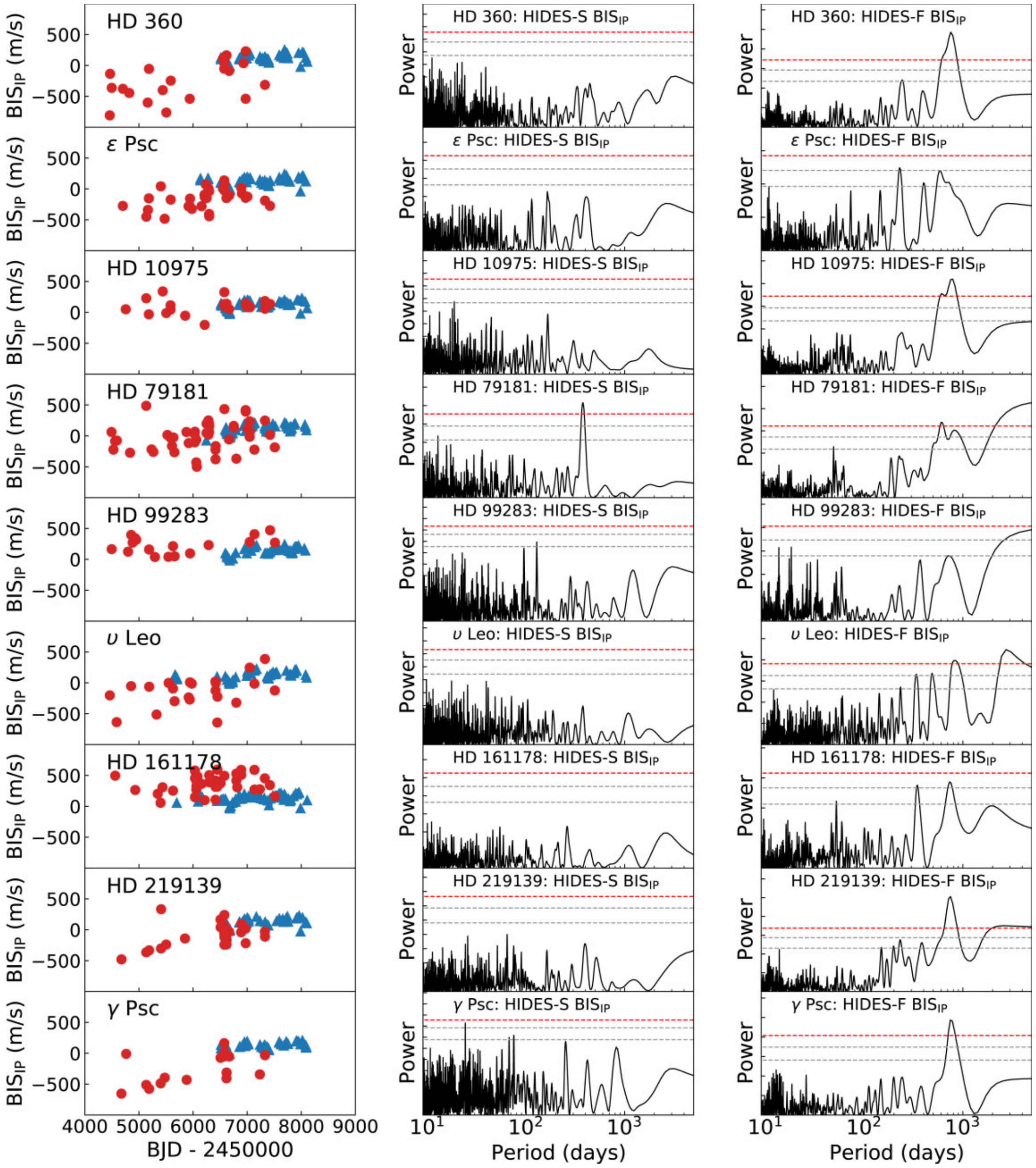

Fig. 10. Left-hand column: $\mathrm{BIS_{IP}}$ variation with time after 2007 December, where red dots are obtained from slit mode spectra (HIDES-S) and blue dots are obtained from fiber mode spectra (HIDES-F). Middle column: GLS of $\mathrm{BIS_{IP}}$ obtained from HIDES-S. Right-hand column: GLS of $\mathrm{BIS_{IP}}$ obtained from HIDES-F. (Color online)

of the main Gaussian envelope is set to be the center of the segment. The effect of IP variation on the line profile was evaluated by Takarada et al. (2018) using the chromospherically inactive G-type giant star ϵ Vir. In their work, they reported that the slit mode spectra of ϵ Vir showed a larger $\mathrm{BIS_{CCF}}$ scatter in a wider velocity range. They did not find a correlation between $\mathrm{BIS_{CCF}}$ and RV, while they found a strong correlation between $\mathrm{BIS_{CCF}}$ and $\mathrm{BIS_{IP}}$ for both slit mode spectra and fiber mode spectra. Therefore, considering the RV variation, e.g., solar-like oscillation and rotational variations, the $\mathrm{BIS_{CCF}}$ of ϵ Vir should reflect the extent of line profile deformation caused by IP variation. Here we remind readers that only data acquired after the CCD extension in 2007 December are viable for $\mathrm{BIS_{CCF}}$ analysis.

In this work, $\mathrm{BIS_{IP}}$ of all nine stars in this work are calculated, and the relation between $\mathrm{BIS_{CCF}}$ and $\mathrm{BIS_{IP}}$ is shown in figure 8. Generally, $\mathrm{BIS_{IP}}$ of fiber mode spectra show higher stability, with mean $\mathrm{BIS_{IP}}$ around $100.0\,\mathrm{m\,s^{-1}}$ and lower rms scatter. In most cases, including HD 360, ϵ Psc, HD 79181, υ Leo, HD 219139, and γ Psc, $\mathrm{BIS_{CCF}}$ of slit mode spectra are generally correlated with $\mathrm{BIS_{IP}}$ (correlation coefficient $|r| \gtrsim 0.6$), and the $\mathrm{BIS_{CCF}}$ of slit mode spectra are on average greater than $\mathrm{BIS_{CCF}}$ of fiber mode spectra.

Therefore, the IP variability is a more dominant factor than line profile in the $\mathrm{BIS_{CCF}}$ variations, and slit mode spectra suffer from IP variation to a greater extent. In the case of HD 161178, however, we do not find strong correlation between $\mathrm{BIS_{CCF}}$ and $\mathrm{BIS_{IP}}$ (correlation coefficient $|r| < 0.23$). Furthermore, the rms of $\mathrm{BIS_{CCF}}$ for both observation modes are almost the same ($16.2\,\mathrm{m\,s^{-1}}$ and $15.0\,\mathrm{m\,s^{-1}}$ for slit mode and fiber mode, respectively). This suggests that stellar modulation is the dominant factor in $\mathrm{BIS_{CCF}}$ rather than $\mathrm{BIS_{IP}}$ for HD 161178. Also, we notice that, for HD 161178, the $\mathrm{BIS_{IP}}$ of slit mode spectra is on average larger and more positive than $\mathrm{BIS_{IP}}$ of fiber mode spectra compared to other stars. As the star is located very close to the north celestial pole on the sky (RA $17^{\rm h}37^{\rm m}08\overset{\rm s}{.}88$, Dec $+72^\circ27'20\overset{''}{.}86$), we infer that it is related to the deformation of the stellar image dependent on the direction to which the telescope points. Therefore, we calculate the mean $\mathrm{BIS_{IP}}$ of slit mode spectra of our nine stars and the mean $\mathrm{BIS_{IP}}$ of slit mode spectra of another 20 stars with Dec $>+60^\circ$ in the Okayama Planet Search Program. Consequently, stars with higher declination tend to have positive and larger $\mathrm{BIS_{IP}}$ values compared to stars located around the celestial equator (figure 9), which verifies our inference of the origin of the stellar image deformation. In the remaining cases, including HD 10975 and HD 99283, the correlation may not be convincing enough since there are fewer slit mode observations for which we can simultaneously obtain both $\mathrm{BIS_{CCF}}$ and $\mathrm{BIS_{IP}}$.

To investigate the IP variation with time, we performed GLS on $\mathrm{BIS_{IP}}$ (figure 10). For $\mathrm{BIS_{IP}}$ of fiber mode spectra, the periodograms show signals at around 600 to 800 d for all the stars. In the case of ϵ Psc, a signal around 400 d might be an explanation for the FWHM regular variation mentioned in section 5. This implies the regular IP variation of fiber mode spectra. For $\mathrm{BIS_{IP}}$ of slit mode spectra, we can by-eye find a general acceleration trend. From periodograms, the IP variation of slit mode spectra seems not to be as regular as the IP variation of fiber mode spectra. However, this might be on account of fewer observation numbers taken by HIDES-S. Peculiarly in the case of HD 79181, the periodogram shows a significant signal at around 377 d, which is close to one year, yet other stars do not show similar variability. As it is more frequently observed than other stars, we infer it might be the true annually instrumental variation.

Appendix 2. Instrumental RV stability

Two RV standard stars were adopted to examine the instrumental stability in RV measurements for this study (figure 11). τ Cet (HD 10700, G8 V, $0.8\,M_\odot$), known to have stable RV among solar-type stars, was set to be one of the RV standard stars in this work. For both observation modes of HIDES, the typical exposure time was set to be 5 min. The rms of HIDES-S was $4.4\,\mathrm{m\,s^{-1}}$, and the rms of HIDES-F was $3.2\,\mathrm{m\,s^{-1}}$. ϵ Vir (HD 113226,

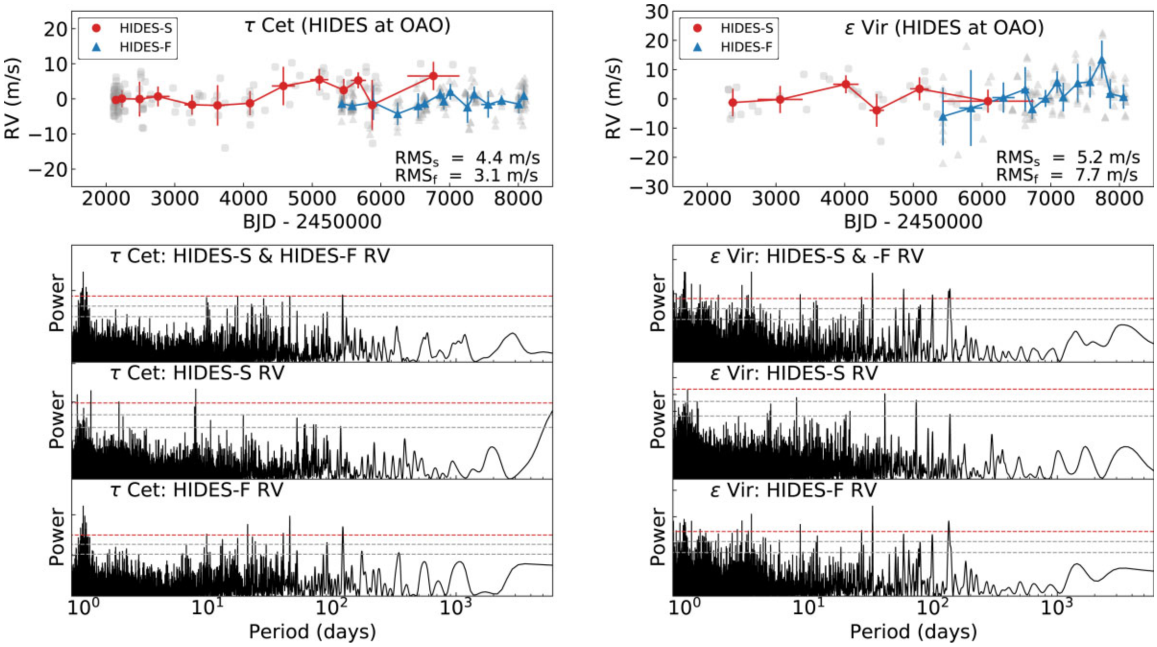

Fig. 11. RV stability of HIDES. The upper panels show the observations for two RV standard stars: τ Cet and ϵ Vir. Colored dots are binned observations, while grey dots in the backgrounds are original observations. Red circular dots indicate HIDES-S observations while blue triangle dots indicate HIDES-F observations. The lower panels show the GLS periodogram of the original RV time series. In GLS periodograms, horizontal lines represent 10%, 1%, and 0.1% FAP level, from bottom to top, respectively.

G8 III, 2.5 $M_\odot$), one of the most RV-stable late-G giant stars among targets in the Okayama Planet Search Program (Sato et al. 2005), was set as a comparison RV standard star. Its stellar mass was re-estimated in the same way as the nine target stars in this study. For both observation modes of HIDES, the typical exposure time was set to be 5 min. The rms of HIDES-S was 5.2 m s^{-1}. As for the rms of HIDES-F, we obtained 7.7 m s^{-1} for all exposures, and 6.7 m s^{-1} for exposures after 2012. Although on average the scatter is larger than τ Cet, this is likely due to the solar-like oscillation. In order to investigate the long-term variation of the instrument, we firstly binned neighboring observations, and each bin was set to be three months at least. If there were less than five observations in a single bin, we combined the next neighboring bin until there were at least five observations in the bin. We calculated the average of time and RV of observations in each bin, and by our educated eyes, we found slight RV variation with time for both stars. Comparing both RV standard stars, τ Cet showed betters RV stability than ϵ Vir. In order to have quantified measurements on long-term variations, we checked periodicity (method: subsection 4.3) in the time series of both RV standard stars. Consequently, we did not find regular variations over 150 d. Therefore, we could rule out regular instrumental variations longer than this period.

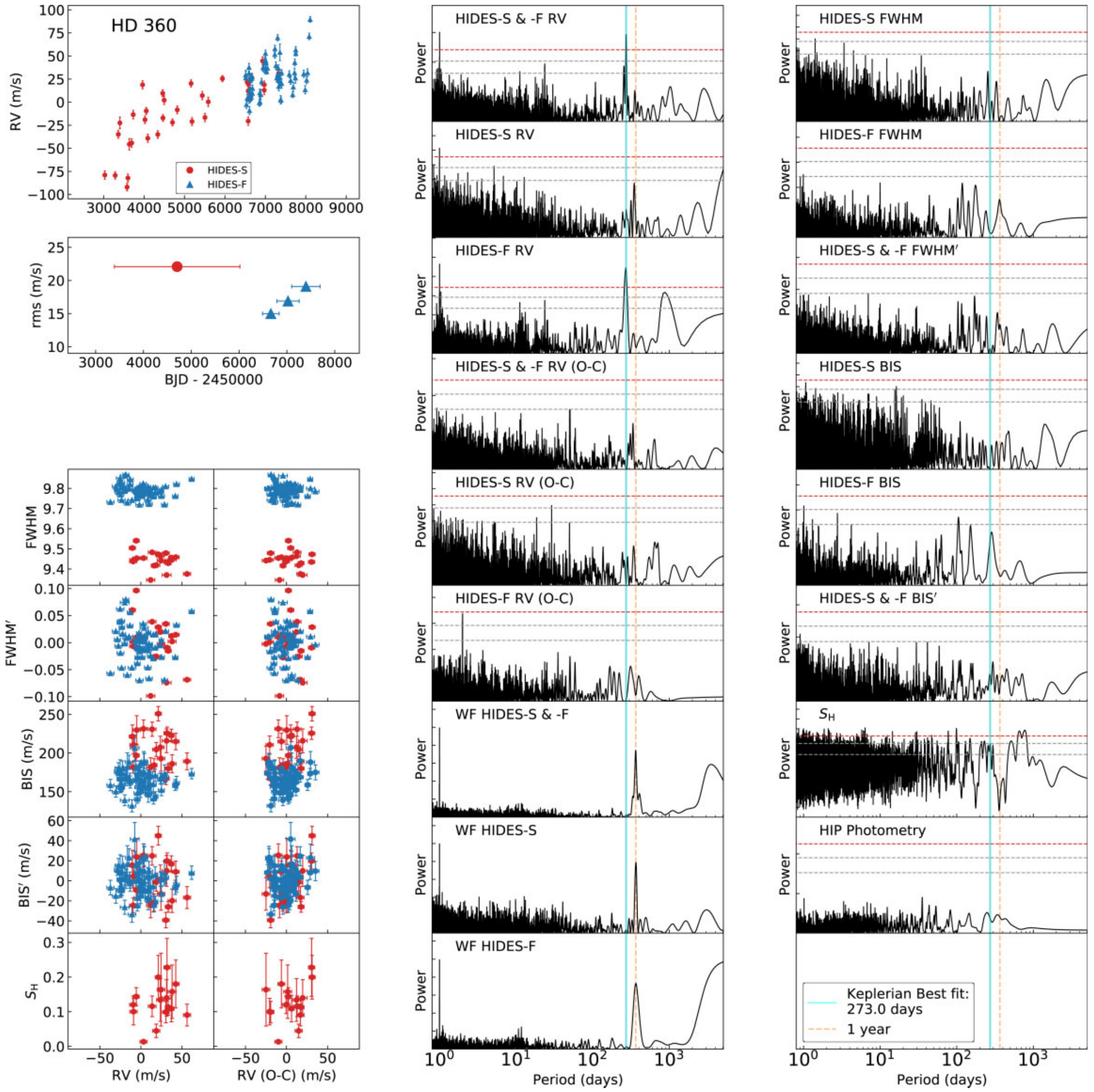

Fig. 12. Summary figure of HD 360. Left-hand column, from top to bottom: RV time series; rms of RVs varying by time; FWHM, FWHM′, BIS, BIS′, and Ca II H index S_H against RVs and RV residuals. Middle column, from top to bottom: GLS periodogram of full RV data, HIDES-S RV data, HIDES-F RV data, full RV residuals, HIDES-S RV residuals, and HIDES-F RV residuals; window function of full RV data, HIDES-S data, and HIDES-F data. Right-hand column, from top to bottom: GLS periodogram of HIDES-S FWHM, HIDES-F FWHM, FWHM′, HIDES-S BIS, HIDES-F BIS, BIS′, Ca II H index S_H, and Hipparcos photometry. In GLS periodograms, the horizontal lines represent 10%, 1%, and 0.1% FAP levels, from bottom to top. The vertical cyan solid line indicates the best-fitted period from the Keplerian model, and the vertical orange dashed line indicates 1 yr. (Color online)

Table 4. Radial velocities of HD 360.

BJD (−2450000)	Radial velocity ($\mathrm{m\,s^{-1}}$)	Uncertainty ($\mathrm{m\,s^{-1}}$)	Observation Mode
3028.8938	−67.4	4.5	HIDES-S
3285.1626	−67.8	3.9	HIDES-S
3362.9977	−23.3	4.3	HIDES-S
3401.9169	−11.0	6.2	HIDES-S
3579.2258	−80.5	4.0	HIDES-S
…	…	…	…

*Only the first five sets of RV data are listed. A complete data listing including RV, FWHM, BIS, and S/N is available online as supplementary data.

Appendix 3. Individual stars

Appendix 3.1 HD 360

We collected a total of 102 data including 35 taken by HIDES-S and 67 taken by HIDES-F between 2004 January and 2017 December. The RV data are shown in figure 12 and the data are listed in table 4. For the full RV data, the GLS periodogram shows one significant peak at 273 d with FAP lower than 0.1%. We did not find significant periodicity with GLS in spectral line profiles or Ca II H index time series, and we did not find RV strongly correlating with either spectral line profiles or Ca II H index ($|r| < 0.4$, where r is the Pearson's correlation coefficient, and r hereafter is likewise defined).[6] We also calculated a periodogram for Hipparcos photometry found no significant periodicity.

We adopted a single Keplerian curve to fit the data and obtained orbital parameters for the companion of $P = 273.1^{+1.6}_{-0.8}$ d, $K = 16.8^{+1.8}_{-2.6}\,\mathrm{m\,s^{-1}}$, and $e = 0.139^{+0.108}_{-0.104}$. The rms scatter of the residuals to the Keplerian fit is $14.8\,\mathrm{m\,s^{-1}}$. We did not find any significant periodicity in the residuals, and we did not find line profiles or Ca II H index strongly correlating with RV residuals ($|r| < 0.4$). Adopting a stellar mass of $M = 1.69\,M_\odot$, we obtained a minimum mass $M_\mathrm{p}\sin i = 0.75^{+0.12}_{-0.15}\,M_\mathrm{J}$ and a semimajor axis $a = 0.98^{+0.11}_{-0.03}$ au for the companion. The phase-folded RV curve is shown in the lower panel in figure 13.

As for HD 360, it shows a significant long-term linear trend, which strongly suggests an outer companion surviving around the host star. The acceleration, which represents the slope of the RV trend, can be used to estimate the minimum of the dynamical mass of the outer body (Winn et al. 2009). By adopting the acceleration of $\dot{\gamma} = 0.018^{+0.002}_{-0.002}\,\mathrm{m\,s^{-1}d^{-1}}$, we obtained

$$\frac{M_\mathrm{c}\sin i_\mathrm{c}}{a_\mathrm{c}^2} \sim \frac{\dot{\gamma}}{G} = 0.037^{+0.004}_{-0.004}\,M_\mathrm{J}\,\mathrm{au}^{-2}, \tag{A1}$$

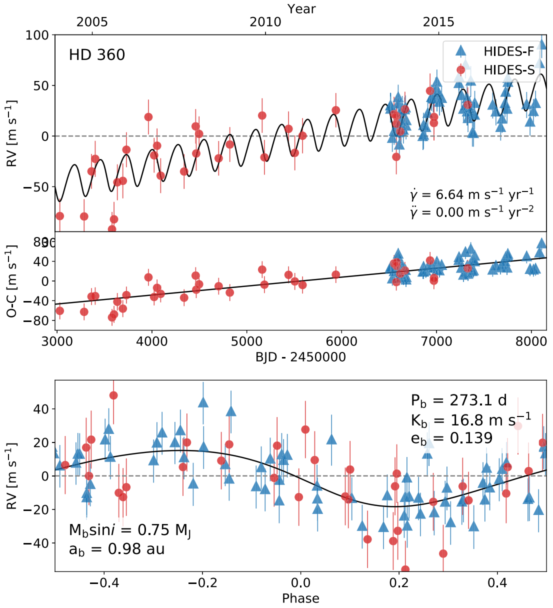

Fig. 13. Orbital solution of HD 360. HIDES-S data are shown in red circles and HIDES-F data are shown in blue triangles. Top: Best-fitting single Keplerian curve in the full time span, with fitted RV offsets between instruments and fitted jitters included in the error bars. Middle: RV residuals to the best fit. Bottom: Phase-folded of top panel. (Color online)

where $\dot{\gamma}$ is the RV acceleration, M_c is the mass of the outer companion, i_c is the orbital inclination, G is the gravitational constant, and a_c is the semimajor axis of the outer companion.

Appendix 3.2 ϵ Psc

We collected a total of 144 data including 60 taken by HIDES-S and 84 taken by HIDES-F between 2002 February and 2017 November. The RV data are shown in figure 14 and the data are listed in table 5. For the full RV data, the GLS periodogram shows two significant peaks with a FAP less than 0.1% including one peak at the period of 247 d (∼2/3 yr) and another peak at a period of 729 d (∼2 yr). The window function shows one peak at 1 yr and another peak over 4000 d. The 1 yr window caused a severe aliasing effect to the true period [noticing $1/2 = 1/(2/3) - 1/1$].

---

[6] Since we only lay emphasis on whether two sets of data correlate with each other or not, but not how they correlate with each other, we here use the absolute value of correlation coefficient r to illustrate the correlation in this work.

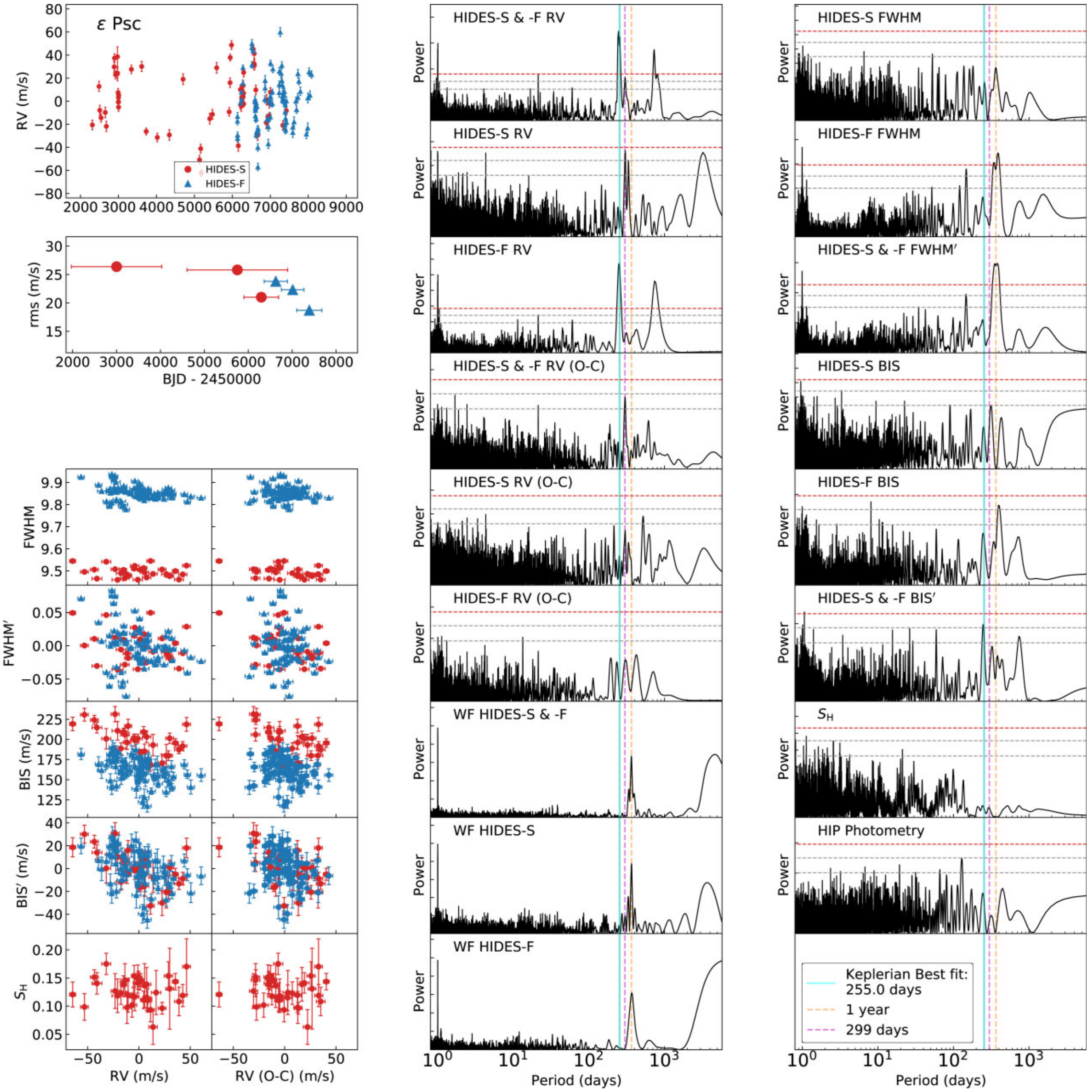

Fig. 14. Summary figure of ϵ Psc. Left-hand column, from top to bottom: RV time series; rms of RVs varying by time; FWHM, FWHM′, BIS, BIS′, and Ca II H index S_H, against RVs and RV residuals. Middle column, from top to bottom: GLS periodogram of full RV data, HIDES-S RV data, HIDES-F RV data, full RV residuals, HIDES-S RV residuals, and HIDES-F RV residuals; window function of full RV data, HIDES-S data, and HIDES-F data. Right-hand column, from top to bottom: GLS periodogram of HIDES-S FWHM, HIDES-F FWHM, FWHM′, HIDES-S BIS, HIDES-F BIS, BIS′, Ca II H index S_H, and Hipparcos photometry. In GLS periodograms, the horizontal lines represent 10%, 1%, and 0.1% FAP levels, from bottom to top. The vertical cyan solid line indicates the best-fitted period from the Keplerian model, the vertical orange dashed line indicates 1 yr, and the vertical pink dashed line indicates the 299 d period of interest. (Color online)

Since the power of the 247 d signal is significantly higher than the 729 d signal, we then confirmed that the 247 d signal should be considered as the true period. The other long-term window is the result of sparse observations in the middle of the HIDES-S baseline. However, it is clear to see that the main peak in the full data GLS is almost dominated by fiber mode data by comparing the GLS periodogram of full data and GLS periodogram of each instrument. We performed SBGLS to investigate the power of different periods, varying by the number of data. In figure 15, it is clear that the power of the 299 d period sharply decreases after 90 observations, which implies the instability of this variation, while the approximately 250 d signals show a more stable increasing power trend. As for the activity indicator, we did not find significant periodicity with GLS in Ca II H index time series, and we did not find RV strongly correlating with fiber mode spectral line profiles or Ca II H index ($|r| \lesssim 0.4$). The FWHM of fiber mode spectra might vary regularly with

Table 5. Radial velocities of ϵ Psc.

BJD (-2450000)	Radial velocity ($\mathrm{m\,s^{-1}}$)	Uncertainty ($\mathrm{m\,s^{-1}}$)	Observation Mode
2311.9252	− 22.9	4.2	HIDES-S
2488.2308	10.5	4.4	HIDES-S
2507.2159	− 10.1	4.3	HIDES-S
2542.0624	− 16.7	3.7	HIDES-S
2652.9970	− 12.0	4.6	HIDES-S
…	…	…	…

*Only the first five sets of RV data are listed. A complete data listing including RV, FWHM, BIS, and S/N is available online as supplementary data.

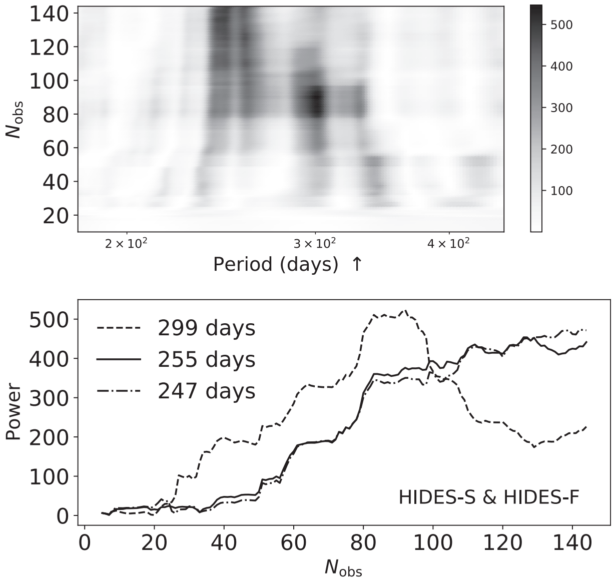

Fig. 15. Stacked Bayesian GLS periodogram of the full data of ϵ Psc. The upper panel shows the power variation with time and the number of data points. The color bar illustrates the strength of power. The lower panel shows the power of interested periods varying with time. The legend of 299 d marked with a dashed line, the legend of 255 d marked with a solid line, and the legend of 247 d marked with dot–dashed line, respectively, represent the periods of interest in the GLS periodogram of RV data.

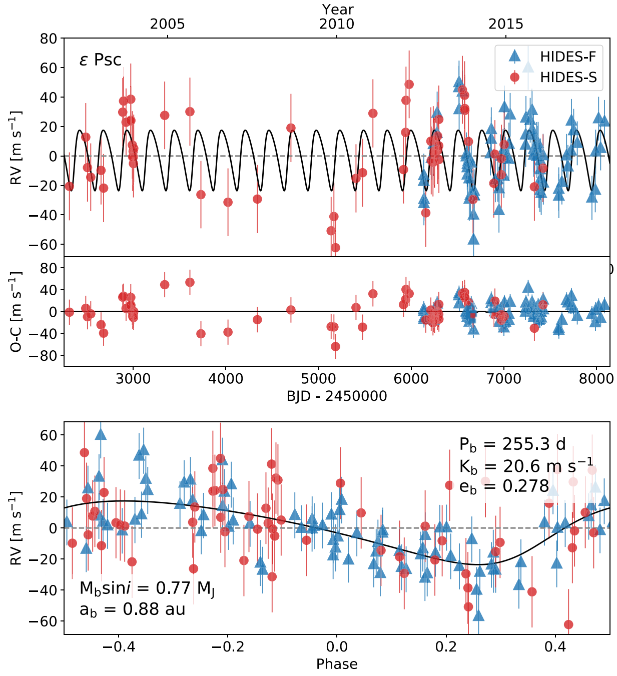

Fig. 16. Orbital solution of ϵ Psc. HIDES-S data are shown in red circles and HIDES-F data are shown in blue triangles. Top: Best-fitting single Keplerian curve in the full time span, with fitted RV offsets between instruments and fitted jitters included in the error bars. Middle: RV residuals to the best fit. Bottom: Phase-folded of top panel.

a period of around 1 yr. We also found a difference in BIS between slit mode and fiber mode spectra. The difference of BIS between slit mode and fiber mode spectra should be similarly caused by IP difference. However, we found RV moderately correlating with BIS of slit mode spectra ($|r| = 0.6$) and BIS′ ($|r| = 0.5$). In the GLS of the BIS time series, we noticed there was a similar periodicity as RV presents for both individual instruments. Therefore, it should be considered that the RV variation may be caused by the star intrinsically. As for Hipparcos photometry, we did not find any significant periodicity.

We adopted a single Keplerian curve to fit the data and obtained orbital parameters for the companion of $P = 255.4^{+2.1}_{-1.4}$ d, $K = 20.6^{+2.1}_{-2.9}\,\mathrm{m\,s^{-1}}$, and $e = 0.057^{+0.159}_{-0.030}$. The rms scatter of the residuals to the Keplerian fit is $18.9\,\mathrm{m\,s^{-1}}$. Adopting a stellar mass of $M = 1.41\,M_\odot$, we obtained a minimum mass $M_{\mathrm{p}} \sin i = 0.77^{+0.14}_{-0.10}\,M_{\mathrm{J}}$ and a semimajor axis $a = 0.88^{+0.11}_{-0.10}$ au for the companion. The phase-folded RV curve is shown in the lower panel in figure 16. The fitted extra noise of HIDES-S is relatively large (larger than semi-amplitude) with a value of $22.7\,\mathrm{m\,s^{-1}}$. The periodicity of 299 d still remains in the full-data residuals although the power of this signal is not high enough (FAP > 1%). Here, we generated mock data in order to test if the 299 d signal could be a fake signal which is mimicked by the true period and noise. We used the true observation window of HIDES-S and the best-fitting Keplerian model of ϵ Psc, and we added random Gaussian noise to the RV time series with the RV jitter derived from the Keplerian fitting. There was a total of 100000 mock time

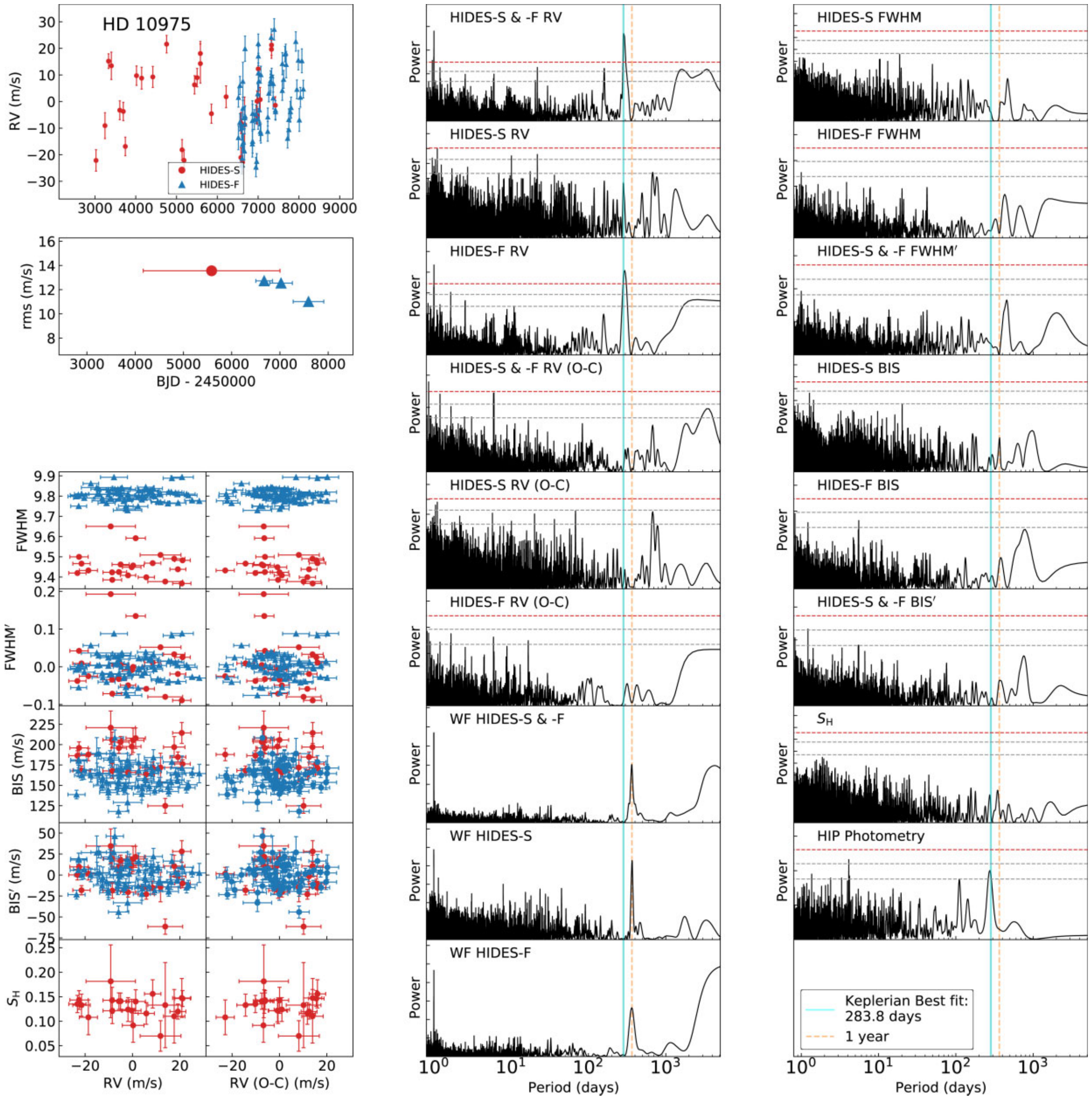

Fig. 17. Summary figure of HD 10975. Left-hand column, from top to bottom: RV time series; rms of RVs varying by time; FWHM, FWHM′, BIS, BIS′, and Ca II H index $S_{\rm H}$, respectively, against RVs and RV residuals. Middle column, from top to bottom: GLS periodogram of full RV data, HIDES-S RV data, HIDES-F RV data, full RV residuals, HIDES-S RV residuals, and HIDES-F RV residuals; window function of full RV data, HIDES-S data, and HIDES-F data. Right-hand column, from top to bottom: GLS periodogram of HIDES-S FWHM, HIDES-F FWHM, FWHM′, HIDES-S BIS, HIDES-F BIS, BIS′, Ca II H index $S_{\rm H}$, and Hipparcos photometry. In GLS periodograms, the horizontal lines represent 10%, 1%, and 0.1% FAP levels, from bottom to top. The vertical cyan solid line indicates the best-fitted period from the Keplerian model, and the vertical orange dashed line indicates 1 yr. (Color online)

series generated, and GLS periodograms were performed to find the periods in the noisy mocked time series. Consequently, 18% of the simulations failed in recognizing the true period (±5% as a criterion), and fake periods could be distributed everywhere in the period phase. In such a case, the 299 d period could be a variation that is either true or triggered by noise. In other words, it is hard to affirm if the period varies with time. Although there are no more accessible observations indicating the RV variation of ϵ Psc is intrinsically triggered by the star, in consideration of moderate correlation and similar periods between RV and BIS we could only label ϵ Psc as a planet-harboring candidate.

Appendix 3.3 HD 10975

We collected a total of 99 data including 32 taken by HIDES-S and 67 taken by HIDES-F between 2004 January

Table 6. Radial velocities of HD 10975.

BJD (−2450000)	Radial velocity (m s^{-1})	Uncertainty (m s^{-1})	Observation Mode
3026.0042	− 22.6	4.1	HIDES-S
3245.2826	− 9.5	4.9	HIDES-S
3333.1050	14.7	2.8	HIDES-S
3401.9937	13.0	5.1	HIDES-S
3608.3144	− 3.7	3.5	HIDES-S
…	…	…	…

*Only the first five sets of RV data are listed. A complete data listing including RV, FWHM, BIS, and S/N is available online as supplementary data.

and 2017 December. The RV data are shown in figure 17 and the data are listed in table 6. For full data, GLS shows a significant peak at the period of 286 d with a FAP of less than 0.1%. We did not find significant periodicity with GLS in Ca II H index time series, and we did not find RV strongly correlating with either spectral line profiles or Ca II H index ($|r| < 0.2$). We also calculated a periodogram for Hipparcos photometry. We could see one weak signal with a similar RV period in the GLS periodogram, yet it is not significant enough (FAP > 1%).

We adopted a single Keplerian curve to fit the data and obtained orbital parameters for the companion of $P = 283.8^{+12.7}_{-0.1}$ d, $K = 12.3^{+0.2}_{-3.5}$ m s^{-1}, and $e = 0.442^{+0.040}_{-0.389}$. The rms scatter of the residuals to the Keplerian fit is 10.7 m s^{-1}. We did not find any significant periodicity in the residuals, and we did not find line profiles or Ca II H index strongly correlating with RV residuals ($|r| < 0.3$). Adopting a stellar mass of $M = 1.41\,M_{\odot}$, we obtained a minimum mass $M_{\mathrm{p}} \sin i = 0.45^{+0.06}_{-0.15}\,M_{\mathrm{J}}$ and a semimajor axis $a = 0.95^{+0.06}_{-0.04}$ au for the companion. The phase-folded RV curve is shown in the lower panel in figure 18.

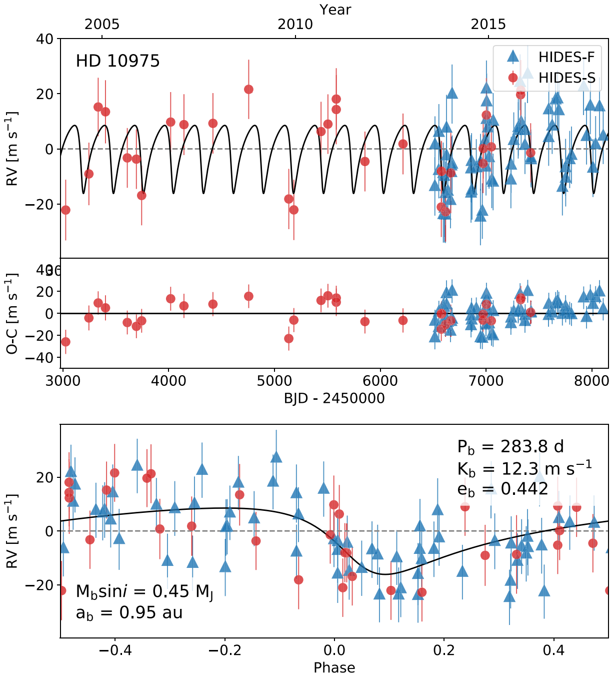

Fig. 18. Orbital solution of HD 10975. HIDES-S data are shown in red circles and HIDES-F data are shown in blue triangles. Top: Best-fitting single Keplerian curve in the full time span, with fitted RV offsets between instruments and fitted jitters included in the error bars. Middle: RV residuals to the best fit. Bottom: Phase-folded of top panel. (Color online)

Appendix 3.4 HD 79181

This star is firstly reported in the result of the first three years Okayama Planet Search Program, yet no planet was detected at that time (Sato et al. 2005). This time, we collected a total of 164 data including 92 taken by HIDES-S and 72 taken by HIDES-F between 2001 March and 2017 December. The RV data are shown in figure 19 and the data are listed in table 7. For full data, the GLS periodogram shows four significant peaks with a FAP of less than 0.1% including peaks at periods of 275, 293, 1119, and 1477 d. The window function shows one peak at 1 yr and another peak over 4000 d. The 1 yr window causes a severe aliasing effect in the period analysis. Recognizing the relations of ($1/1119 \simeq 1/275 - 1/365$) and ($1/1477 \simeq 1/293 - 1/365$), we therefore confirmed that periods of 1119 and 1477 d should be classified as the aliases of 275 and 293 d, respectively. The other long-term window is the result of sparse observations in the middle of the HIDES-S baseline and it also causes aliasing on the true signal. Either 275 d or 293 d is the alias of the other one. Since full RV data and HIDES-S RV data show different stronger signals, and HIDES-F RV data show only one peak, we performed SBGLS to investigate the signal closer to the true period in the periodogram. Consequently, SBGLS shows that significant periodicity appears after 100 observations, and the power of 275 d becomes apparently stronger than the power of 293 d after gathering 145 observations (figure 20). There is one signal at around 1 yr in the periodograms of BIS for slit mode spectra. According to the IP discussion in appendix 1, we confirm they are regular instrumental variations. There are another two signals at 254 d and 812 d

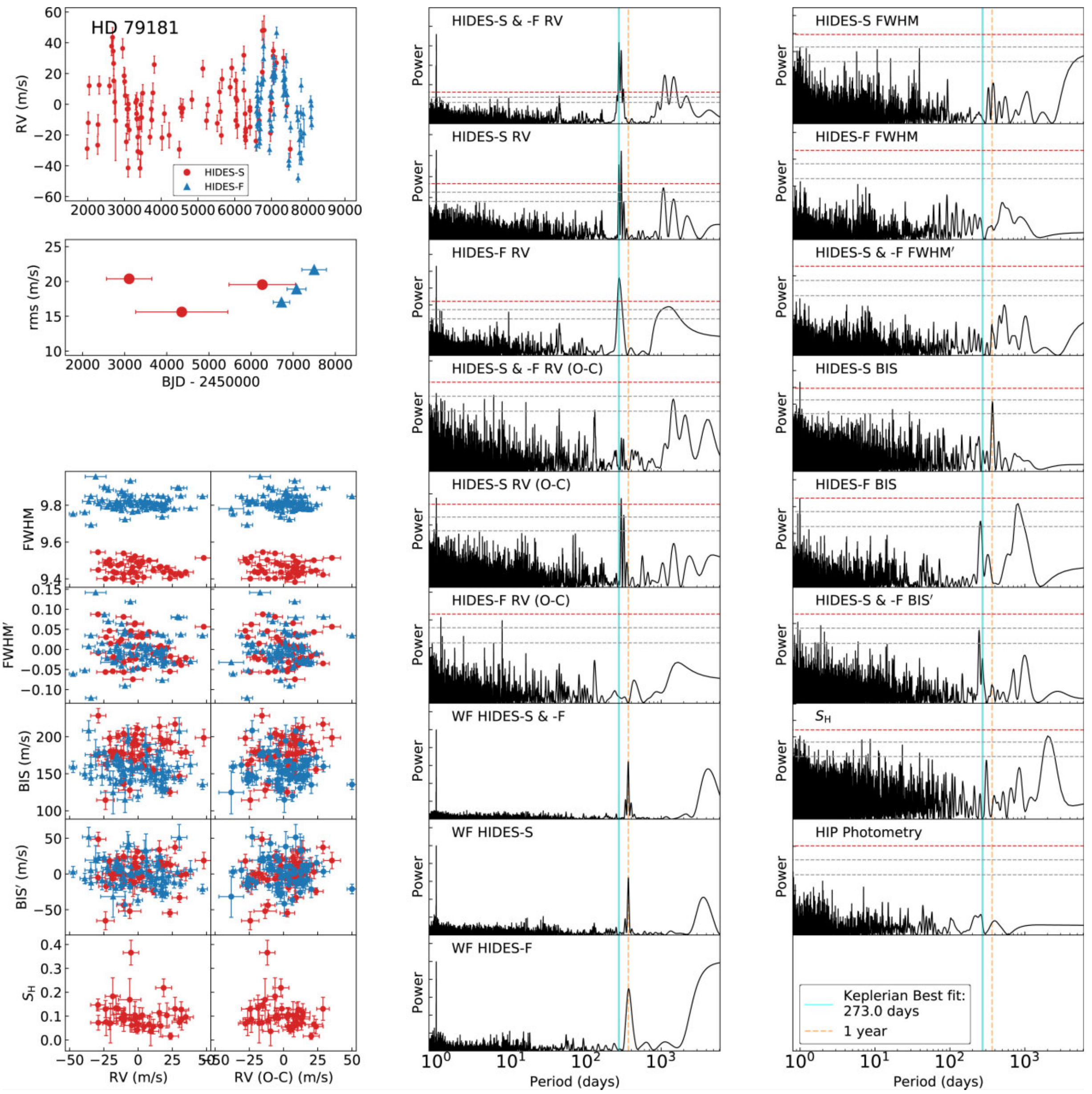

Fig. 19. Summary figure of HD 79181. Left-hand column, from top to bottom: RV time series; rms of RVs varying by time; FWHM, FWHM′, BIS, BIS′, and Ca II H index S_{H}, respectively, against RVs and RV residuals. Middle column, from top to bottom: GLS periodogram of full RV data, HIDES-S RV data, HIDES-F RV data, full RV residuals, HIDES-S RV residuals, and HIDES-F RV residuals; window function of full RV data, HIDES-S data, and HIDES-F data. Right-hand column, from top to bottom: GLS periodogram of HIDES-S FWHM, HIDES-F FWHM, FWHM′, HIDES-S BIS, HIDES-F BIS, BIS′, Ca II H index S_{H}, and Hipparcos photometry. In GLS periodograms, the horizontal lines represent 10%, 1%, and 0.1% FAP levels, from bottom to top. The vertical cyan solid line indicates the best-fitted period from the Keplerian model, and the vertical orange dashed line indicates 1 yr. (Color online)

in the periodograms of BIS for fiber mode spectra and BIS′ for both spectra. Recognizing ($1/254 \simeq 1/812 + 1/365$), we therefore determined that the 254 d signal should be the alias. We did not find significant periodicity with GLS in Ca II H index time series, and we did not find RV strongly correlating with either spectral line profiles or Ca II H index ($|r| \lesssim 0.2$).

We adopted a single Keplerian curve to fit the data and obtained orbital parameters for the companion of $P = 273.1^{+1.3}_{-0.4}$ d, $K = 17.7^{+1.6}_{-2.2}\,\mathrm{m\,s^{-1}}$, and $e = 0.259^{+0.067}_{-0.206}$. The rms scatter of the residuals to the Keplerian fit is $15.5\,\mathrm{m\,s^{-1}}$. We find a relatively significant signal at 292 d in the residuals of data taken by only HIDES-S. Since the period of this regular variation is almost the same as the one detected from the original RV taken by HIDES-S, it implies that the 293 d variation cannot be fully subtracted. In such a case, we infer that sparse observation of HIDES-S could account for the inaccuracy in searching for the true

Table 7. Radial velocities of HD 79181.

BJD (−2450000)	Radial velocity (m s^{-1})	Uncertainty (m s^{-1})	Observation Mode
1987.0079	− 28.7	6.5	HIDES-S
2016.0188	− 11.9	6.8	HIDES-S
2041.9640	12.2	6.0	HIDES-S
2272.3077	− 26.5	5.9	HIDES-S
2282.2919	− 13.1	6.5	HIDES-S
...	...	...	...

*Only the first five sets of RV data are listed. A complete data listing including RV, FWHM, BIS, and S/N is available online as supplementary data.

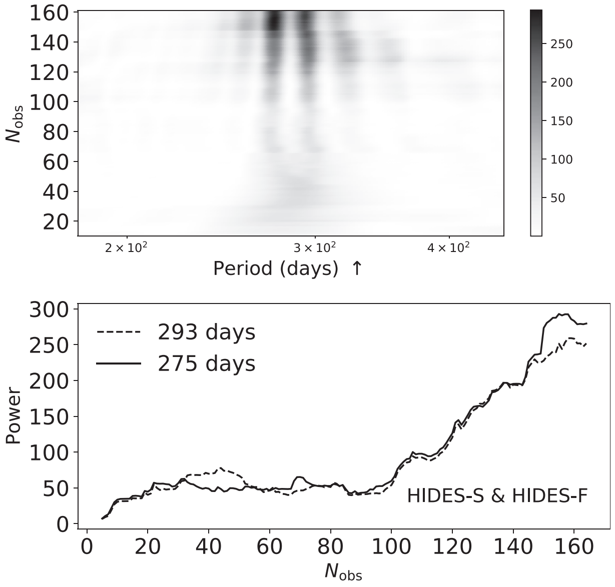

Fig. 20. Stacked Bayesian GLS periodogram of the full data of HD 79181. The upper panel shows the power variation with time and the number of data points. The color bar illustrates the strength of power. The lower panel shows the power of interested periods varying with time. The legend of 293 d marked with a dashed line and the legend of 275 d marked with a solid line respectively represent the periods of interest of the 293 d signal and the 275 d signal in the GLS periodogram of RV data. (Color online)

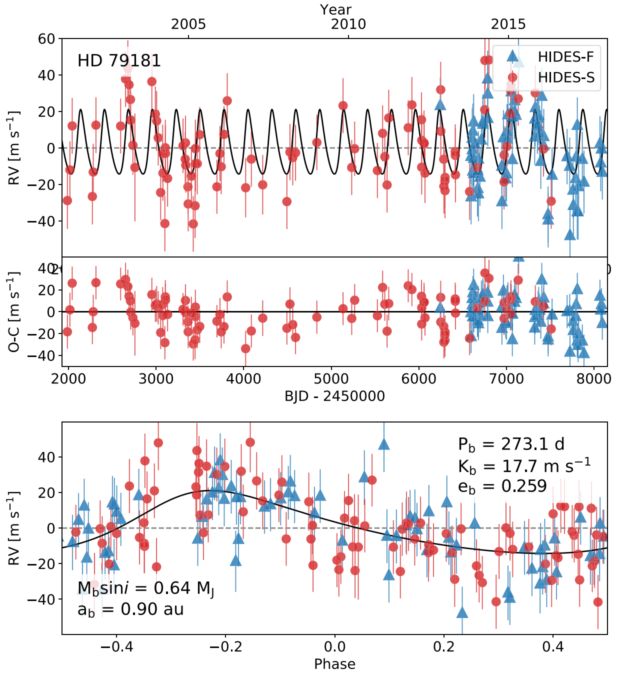

Fig. 21. Orbital solution of HD 79181. HIDES-S data are shown in red circles and HIDES-F data are shown in blue triangles. Top: Best-fitting single Keplerian curve in the full time span, with fitted RV offsets between instruments and fitted jitters included in the error bars. Middle: RV residuals to the best fit. Bottom: Phase-folded of top panel. (Color online)

period. As for the activity indicators, we did not find line profiles or Ca II H index strongly correlating with RV residuals ($|r| < 0.3$). In this case, it is confident to say that the period of 273 d, rather than 293 d, is the true orbital period. Adopting a stellar mass of $M = 1.28\,M_{\odot}$, we obtained a minimum mass $M_{\mathrm{p}}\sin i = 0.64^{+0.06}_{-0.16}\,M_{\mathrm{J}}$ and a semimajor axis $a = 0.90^{+0.07}_{-0.08}$ au for the companion. The phase-folded RV curve is shown in the lower panel in figure 21.

Appendix 3.5 HD 99283

We collected a total of 82 data including 28 taken by HIDES-S and 54 taken by HIDES-F between 2004 January and 2017 November. The RV data are shown in figure 22 and the data are listed in table 8. The GLS shows a significant peak at the period of 310 d with a FAP of less than 0.1%. We did not find significant periodicity with GLS in Ca II H index time series, and we did not find RV strongly correlating with either spectral line profiles or Ca II H index ($|r| < 0.3$).

We adopted a single Keplerian curve to fit the data and obtained orbital parameters for the companion of $P = 310.4^{+5.2}_{-1.7}$ d, $K = 20.4^{+1.9}_{-3.5}$ m s^{-1}, and $e = 0.200^{+0.102}_{-0.146}$. The rms scatter of the residuals to the Keplerian fit is 14.4 m s^{-1}. We did not find any significant periodicity in the residuals, and we did not find line profiles or Ca II H index strongly correlating with RV residuals ($|r| < 0.2$). Adopting a stellar mass of $M = 1.76\,M_{\odot}$, we obtained

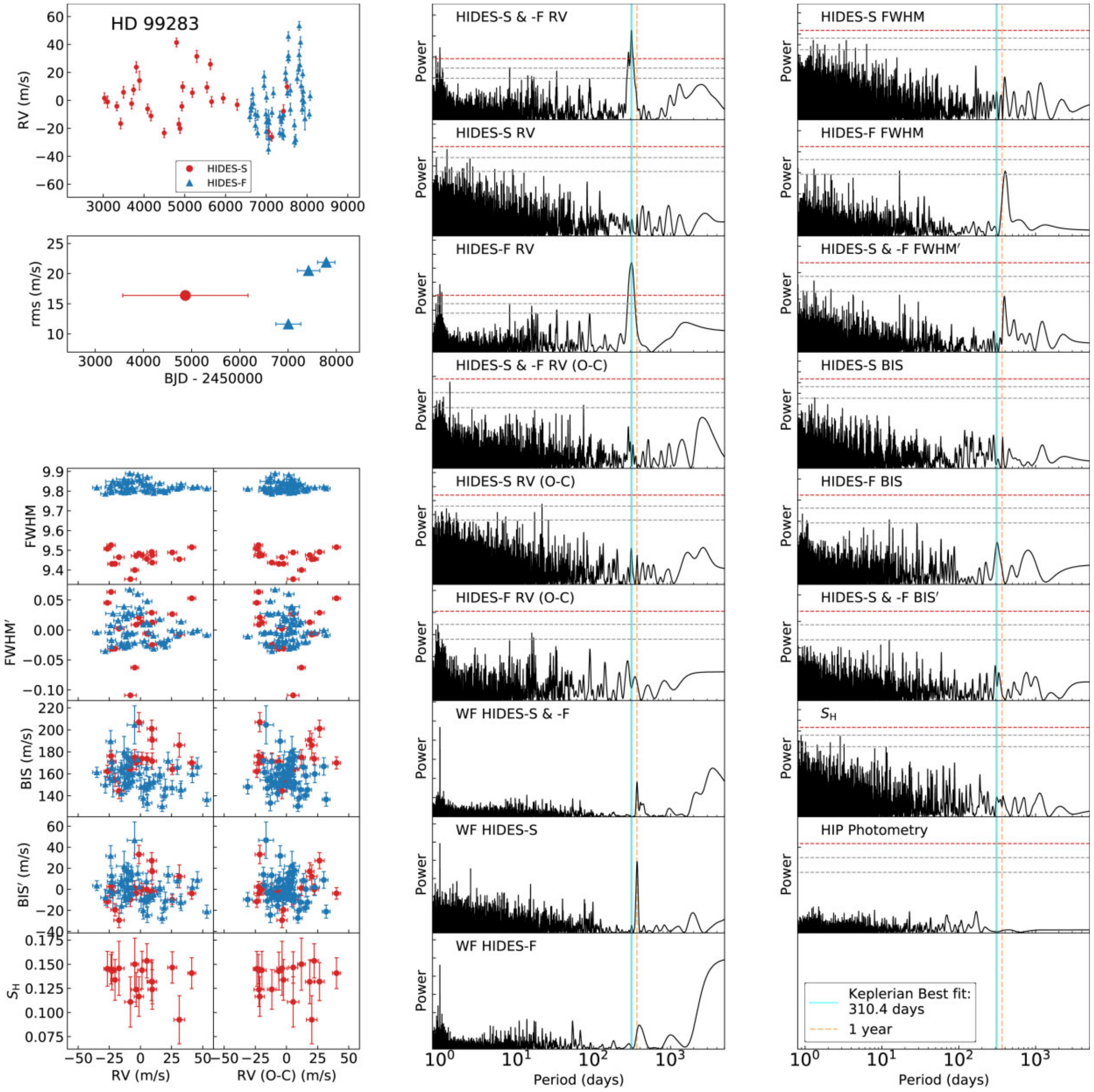

Fig. 22. Summary figure of HD 99283. Left-hand column, from top to bottom: RV time series; rms of RVs varying by time; FWHM, FWHM′, BIS, BIS′, and Ca II H index $S_{\rm H}$, respectively, against RVs and RV residuals. Middle column, from top to bottom: GLS periodogram of full RV data, HIDES-S RV data, HIDES-F RV data, full RV residuals, HIDES-S RV residuals, and HIDES-F RV residuals; window function of full RV data, HIDES-S data, and HIDES-F data. Right-hand column, from top to bottom: GLS periodogram of HIDES-S FWHM, HIDES-F FWHM, FWHM′, HIDES-S BIS, HIDES-F BIS, BIS′, Ca II H index $S_{\rm H}$, and Hipparcos photometry. In GLS periodograms, the horizontal lines represent 10%, 1%, and 0.1% FAP level from bottom to top. The vertical cyan solid line indicates the best-fitted period from the Keplerian model, and the vertical orange dashed line indicates 1 yr. (Color online)

a minimum mass $M_{\rm p}\sin i = 0.97^{+0.06}_{-0.25}\,M_{\rm J}$ and a semimajor axis $a = 1.08^{+0.07}_{-0.05}$ au for the companion. We also present RV scatters varying with time in figure 22. From the figure, we can find that the first scatter measurement of HIDES-F is apparently lower than the other three measurements. Combining this with the result from Keplerian fitting, we can know that the data included by the first scatter measurement of HIDES-F is mainly located on the second half of the orbital phase, which refers to the phase between 0 and 0.5 in the bottom panel in figure 23. For the other three scatter measurements, by considering solar-like oscillations and instrumental jitter, we believe the scatter of rms is acceptable as these rms measurements are located around $20\,\mathrm{m\,s^{-1}}$.

Appendix 3.6 υ Leo

We collected a total of 105 data including 46 taken by HIDES-S and 59 taken by HIDES-F between 2001 December and 2017 November. The RV data are shown in

Table 8. Radial velocities of HD 99283.

BJD (−2450000)	Radial velocity ($\mathrm{m\,s^{-1}}$)	Uncertainty ($\mathrm{m\,s^{-1}}$)	Observation Mode
3030.2885	1.3	3.8	HIDES-S
3105.1390	− 1.3	4.2	HIDES-S
3333.2632	− 4.4	3.1	HIDES-S
3428.1573	− 16.8	3.8	HIDES-S
3498.0961	5.5	4.1	HIDES-S
...	...	...	...

*Only the first five sets of RV data are listed. A complete data listing including RV, FWHM, BIS, and S/N is available online as supplementary data.

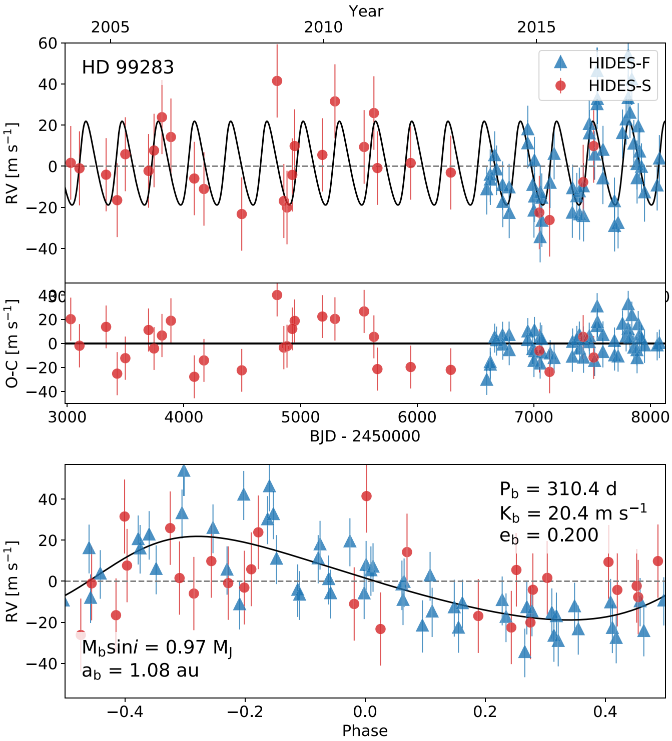

Fig. 23. Orbital solution of HD 99283. HIDES-S data are shown in red circles and HIDES-F data are shown in blue triangles. Top: Best-fitting single Keplerian curve in the full time span, with fitted RV offsets between instruments and fitted jitters included in the error bars. Middle: RV residuals to the best fit. Bottom: Phase-folded of top panel. (Color online)

figure 24 and the data are listed in table 9. The GLS shows a significant peak at the period of 387 d with a FAP of less than 0.1%. Although a signal at 527 d derived from Ca II H index time series might indicate the rotational period, we did not find RV strongly correlating with either spectral line profiles or Ca II H index ($|r| < 0.5$). We did not find RV correlating with line profiles.

We adopted a single Keplerian curve to fit the data and obtained orbital parameters for the companion of $P = 385.2^{+2.8}_{-1.3}$ d, $K = 11.7^{+1.9}_{-3.5}\,\mathrm{m\,s^{-1}}$, and $e = 0.320^{+0.134}_{-0.218}$. The rms scatter of the residuals to the Keplerian fit is $11.2\,\mathrm{m\,s^{-1}}$. The fitted extra noise of HIDES-S is relatively large (larger than semi-amplitude) with a value of $12.5\,\mathrm{m\,s^{-1}}$. We did not find any significant periodicity in the residuals, and we did not find line profiles or Ca II H index strongly correlating with RV residuals ($|r| < 0.5$). Adopting a stellar mass of $M = 1.48\,M_{\odot}$, we obtained a minimum mass $M_{\mathrm{p}} \sin i = 0.51^{+0.06}_{-0.25}\,M_{\mathrm{J}}$ and a semimajor axis $a = 1.18^{+0.07}_{-0.05}$ au for the companion. We also present RV scatters varying with time in figure 24. We find that the scatters of HIDES-S data are lower than the ones of HIDES-F data. However, we also notice that the data included in the second and third scatter measurements of HIDES-F observations are mainly located at the first half of the orbital phase (phase between −0.5 and 0 in the bottom panel of figure 25). In such a case, we could know that the low scatter of HIDES-F data was due to the observational window along the observation baseline.

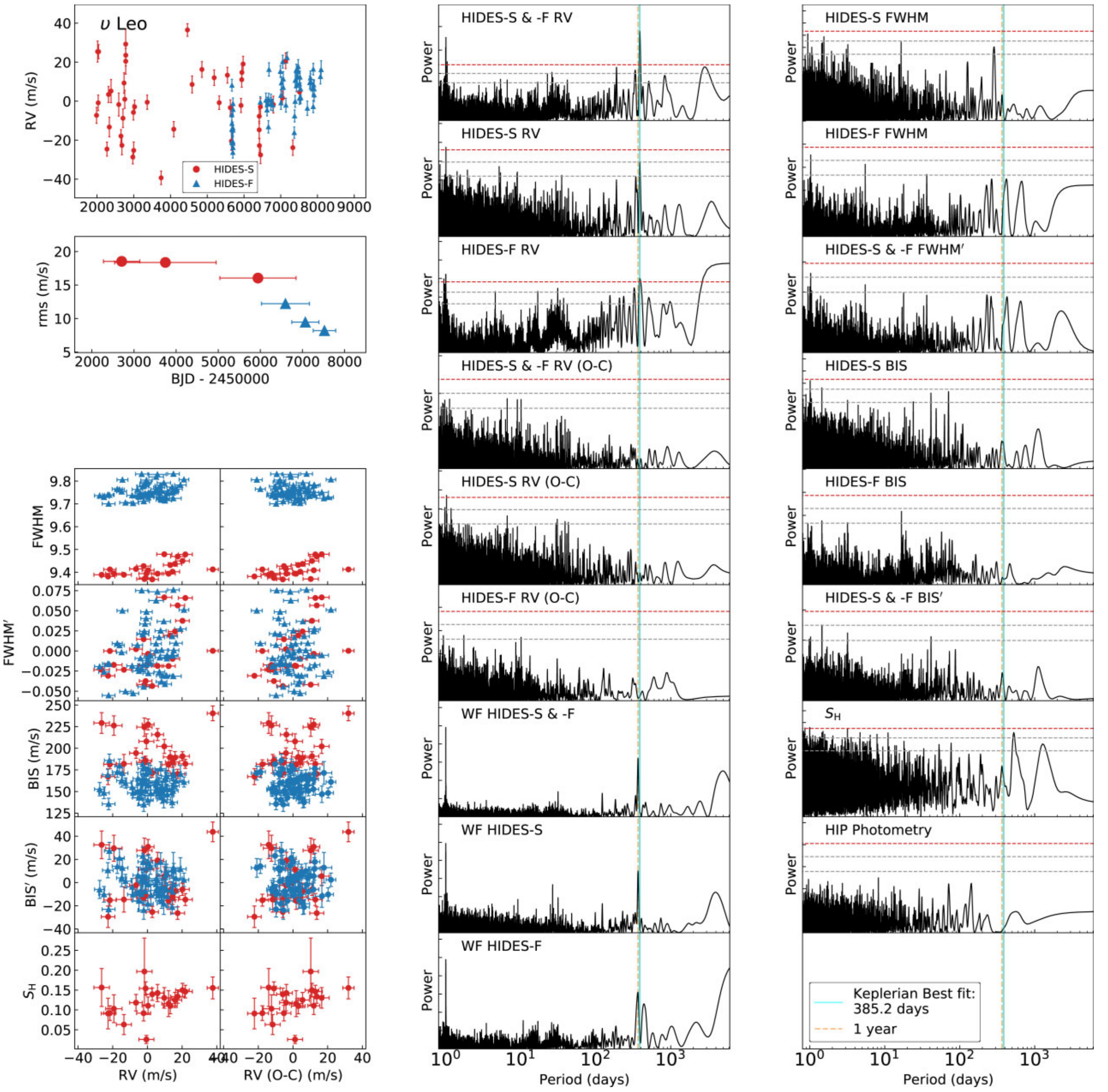

Fig. 24. Summary figure of υ Leo. Left-hand column, from top to bottom: RV time series; rms of RVs varying by time; FWHM, FWHM′, BIS, BIS′, and Ca II H index $S_{\rm H}$, respectively, against RVs and RV residuals. Middle column, from top to bottom: GLS periodogram of full RV data, HIDES-S RV data, HIDES-F RV data, full RV residuals, HIDES-S RV residuals, and HIDES-F RV residuals; window function of full RV data, HIDES-S data, and HIDES-F data. Right-hand column, from top to bottom: GLS periodogram of HIDES-S FWHM, HIDES-F FWHM, FWHM′, HIDES-S BIS, HIDES-F BIS, BIS′, Ca II H index $S_{\rm H}$, and Hipparcos photometry. In GLS periodograms, the horizontal lines represent 10%, 1%, and 0.1% FAP level from bottom to top. The vertical cyan solid line indicates the best-fitted period from the Keplerian model, and the vertical orange dashed line indicates 1 yr. (Color online)

Appendix 3.7 HD 161178

This star was first reported in the result of the first three years of the Okayama Planet Search Program, yet no planet was detected at that time (Sato et al. 2005). This time, we collected a total of 154 data including 77 taken by HIDES-S and 77 taken by HIDES-F between 2001 March and 2017 December. The RV data are shown in figure 26 and the data are listed in table 10. The generalized Lomb–Scargle periodogram shows three significant peaks with a FAP of less than 0.1% including peaks at periods of 263, 279, and 297 d for full data. This is the aliasing effect by a strong window at around 6000 d. This window function is the result of sparse observation in the middle of the HIDES-S baseline. Since full RV data and HIDES-S RV data show different strongest signals, and HIDES-F RV data show only one peak in the periodogram, we performed SBGLS to investigate the signal in the neighboring period region. Consequently, the SBGLS periodogram shows that the power

Table 9. Radial velocities of υ Leo.

BJD (−2450000)	Radial velocity (m s^{-1})	Uncertainty (m s^{-1})	Observation Mode
1987.2705	− 6.1	4.1	HIDES-S
2016.1508	26.6	5.4	HIDES-S
2033.0790	0.3	4.0	HIDES-S
2043.0306	26.5	3.6	HIDES-S
2271.2775	− 23.4	3.6	HIDES-S
...	...	...	...

*Only the first five sets of RV data are listed. A complete data listing including RV, FWHM, BIS, and S/N is available online as supplementary data.

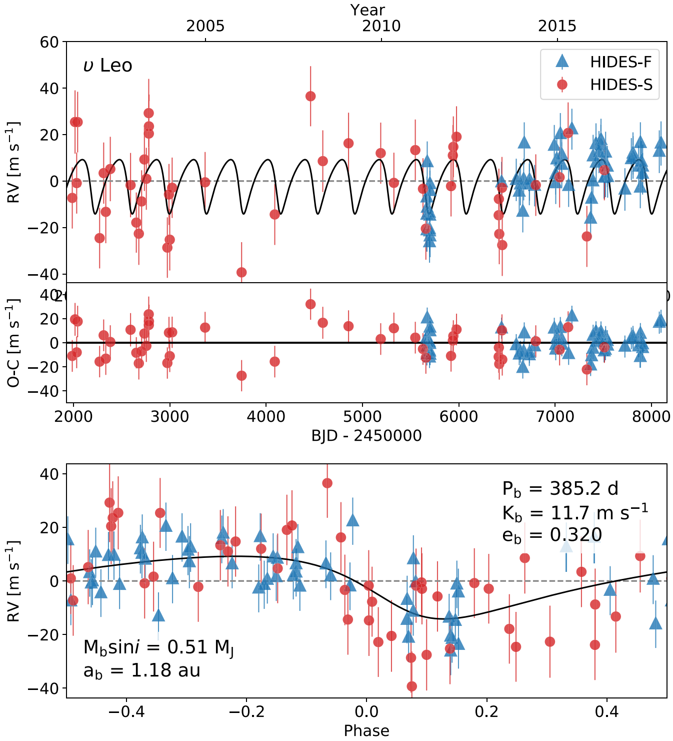

Fig. 25. Orbital solution of υ Leo. HIDES-S data are shown in red circles and HIDES-F data are shown in blue triangles. Top: Best-fitting single Keplerian curve in the full time span, with fitted RV offsets between instruments and fitted jitters included in the error bars. Middle: RV residuals to the best fit. Bottom: Phase-folded of top panel. (Color online)

of 279 d becomes the strongest one after 125 observations (figure 27). Here, we also notice a slight power decreases for all these three peaks after about 125 observations. This could probably be introduced by jitters, and it calls for our attention in future follow-up observations. Furthermore, we did not find significant periodicity with GLS in line profiles and Ca II H index time series, and we did not find RV strongly correlating with either spectral line profiles or Ca II H index ($|r| < 0.2$).

We adopted a single Keplerian curve to fit the data and obtained orbital parameters for the companion of $P = 279.3^{+1.0}_{-0.8}$ d, $K = 17.0^{+1.0}_{-0.8}$ m s^{-1}, and $e = 0.044^{+0.132}_{-0.019}$. The rms scatter of the residuals to the Keplerian fit is 16.0 m s^{-1}. We did not find any significant periodicity in the residuals. In this case, we can be confident in saying that the period of 279 d, rather than 269 or 297 d, is the true orbital period, and we did not find line profiles or Ca II H index strongly correlating with RV residuals ($|r| < 0.2$). By adopting a stellar mass of $M = 1.05\,M_\odot$, we obtained a minimum mass $M_\mathrm{p} \sin i = 0.57^{+0.02}_{-0.16}\,M_\mathrm{J}$ and a semimajor axis $a = 0.85^{+0.05}_{-0.07}$ au for the companion. The phase-folded RV curve is shown in the lower panel in figure 28.

Appendix 3.8 HD 219139

We collected a total of 111 data including 42 taken by HIDES-S and 69 taken by HIDES-F between 2004 January and 2017 December. The RV data are shown in figure 29

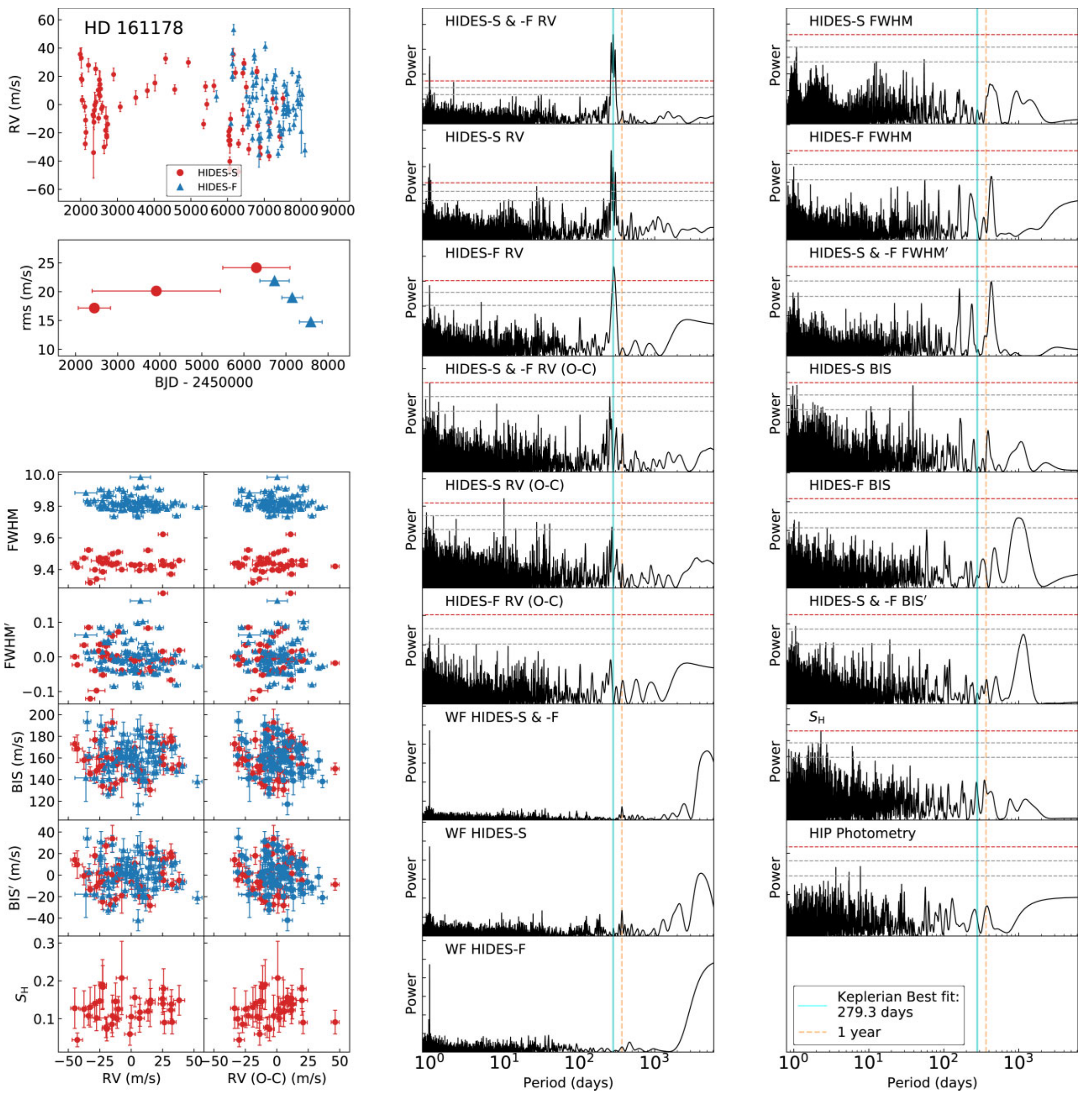

Fig. 26. Summary figure of HD 161178. Left-hand column, from top to bottom: RV time series; rms of RVs varying by time; FWHM, FWHM′, BIS, BIS′, and Ca II H index S_H, respectively, against RVs and RV residuals. Middle column, from top to bottom: GLS periodogram of full RV data, HIDES-S RV data, HIDES-F RV data, full RV residuals, HIDES-S RV residuals, and HIDES-F RV residuals; window function of full RV data, HIDES-S data, and HIDES-F data. Right-hand column, from top to bottom: GLS periodogram of HIDES-S FWHM, HIDES-F FWHM, FWHM′, HIDES-S BIS, HIDES-F BIS, BIS′, Ca II H index S_H, and Hipparcos photometry. In GLS periodograms, the horizontal lines represent 10%, 1%, and 0.1% FAP levels, from bottom to top. The vertical cyan solid line indicates the best-fitted period from the Keplerian model, and the vertical orange dashed line indicates 1 yr. (Color online)

and the data are listed in table 11. The GLS shows a significant peak at the period of 276 d with a FAP of less than 0.1%, and another significant signal located at 1153 d. Recognizing the relations of ($1/1153 \simeq 1/276 - 1/365$), we are aware that the 1153 d signal is an alias caused by the 1 yr window function. For further investigation of periodicity, we did not find significant periodicity with GLS in line profiles or Ca II H index time series, and we did not find RV strongly correlating with either spectral line profiles or Ca II H index ($|r| < 0.3$).

We adopted a single Keplerian curve to fit the data and obtained orbital parameters for the companion of $P = 275.5^{+2.3}_{-1.0}$ d, $K = 19.2^{+1.8}_{-2.6}$ m s^{-1}, and $e = 0.110^{+0.087}_{-0.081}$. The rms scatter of the residuals to the Keplerian fit is

Table 10. Radial velocities of HD 161178.

BJD (−2450000)	Radial velocity ($\mathrm{m\,s^{-1}}$)	Uncertainty ($\mathrm{m\,s^{-1}}$)	Observation Mode
1987.3376	38.3	4.3	HIDES-S
2016.2007	35.7	7.2	HIDES-S
2018.2127	20.9	2.9	HIDES-S
2036.1503	20.3	4.7	HIDES-S
2041.2751	5.7	2.9	HIDES-S
…	…	…	…

*Only the first five sets of RV data are listed. A complete data listing including RV, FWHM, BIS, and S/N is available online as supplementary data.

Table 11. Radial velocities of HD 219139.

BJD (−2450000)	Radial velocity ($\mathrm{m\,s^{-1}}$)	Uncertainty ($\mathrm{m\,s^{-1}}$)	Observation Mode
3025.8918	9.7	4.5	HIDES-S
3245.2039	8.6	3.7	HIDES-S
3332.0253	26.8	3.4	HIDES-S
3582.2343	− 23.9	6.7	HIDES-S
3656.1926	− 12.6	3.6	HIDES-S
…	…	…	…

*Only the first five sets of RV data are listed. A complete data listing including RV, FWHM, BIS, and S/N is available online as supplementary data.

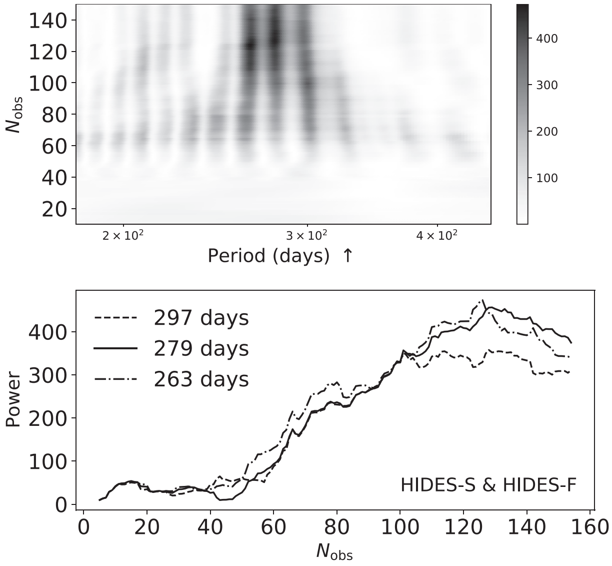

Fig. 27. Stacked Bayesian GLS periodogram of the full data of HD 161178. The upper panel shows the power variation with time and the number of data points. The color bar illustrates the strength of power. The lower panel shows the power of the periods of interest, varying with time. The legend of 297 d marked with a dashed line, the legend of 279 d marked with a solid line, and the legend of 263 d marked with dot–dashed line respectively represent the periods of interest of the 297 d signal, the 279 d signal, and the 275 d signal in the GLS periodogram of RV data.

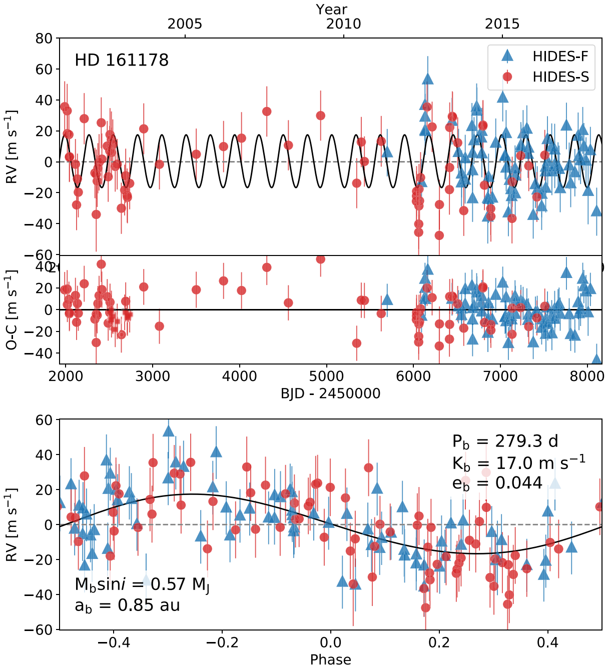

Fig. 28. Orbital solution of HD 161178. HIDES-S data are shown in red circles and HIDES-F data are shown in blue triangles. Top: Best-fitting single Keplerian curve in the full time span, with fitted RV offsets between instruments and fitted jitters included in the error bars. Middle: RV residuals to the best fit. Bottom: Phase-folded of top panel. (Color online)

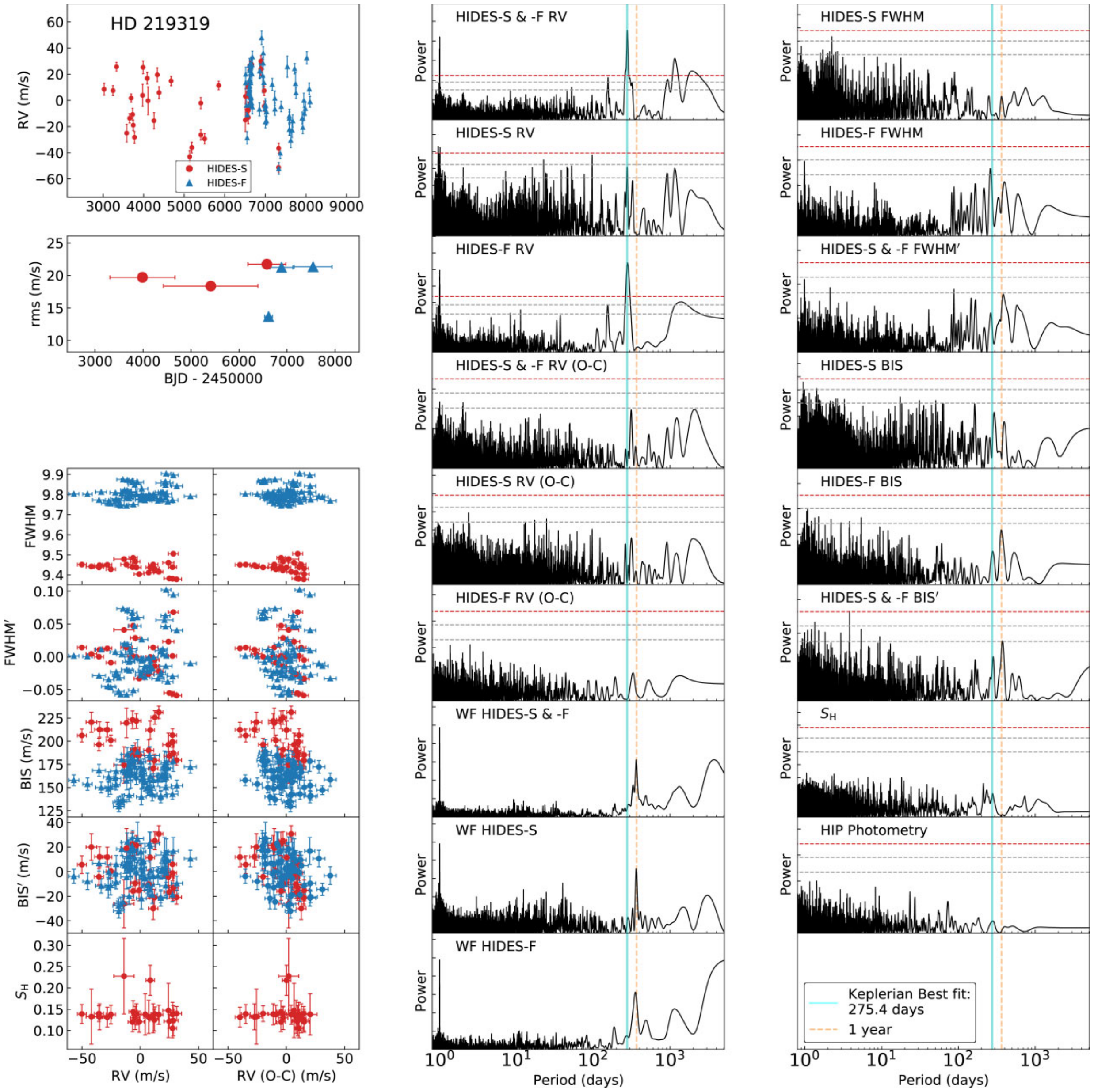

Fig. 29. Summary figure of HD219139. Left-hand column, from top to bottom: RV time series; rms of RVs varying by time; FWHM, FWHM′, BIS, BIS′, and Ca II H index S_{H}, respectively, against RVs and RV residuals. Middle column, from top to bottom: GLS periodogram of full RV data, HIDES-S RV data, HIDES-F RV data, full RV residuals, HIDES-S RV residuals, and HIDES-F RV residuals; window function of full RV data, HIDES-S data, and HIDES-F data. Right-hand column, from top to bottom: GLS periodogram of HIDES-S FWHM, HIDES-F FWHM, FWHM′, HIDES-S BIS, HIDES-F BIS, BIS′, Ca II H index S_{H}, and Hipparcos photometry. In GLS periodograms, the horizontal lines represent 10%, 1%, and 0.1% FAP level from bottom to top. The vertical cyan solid line indicates the best-fitted period from the Keplerian model, and the vertical orange dashed line indicates 1 yr. (Color online)

$15.1\,\mathrm{m\,s^{-1}}$. We did not find any significant periodicity in the residuals, and we did not find line profiles or Ca II H index strongly correlating with RV residuals ($|r| < 0.5$). Adopting a stellar mass of $M = 1.46\,M_{\odot}$, we obtained a minimum mass $M_{\mathrm{p}} \sin i = 0.78^{+0.05}_{-0.20}\,M_{\mathrm{J}}$ and a semimajor axis $a = 0.94^{+0.06}_{-0.05}$ au for the companion. We also present RV scatters varying with time in figure 29. Combining with the result from Keplerian fitting, we know that the data included by the first scatter measurement of HIDES-F is mainly located on the first half in the orbital phase (phase between −0.5 and 0 in the lower panel in figure 30). For these other scatter measurements, by considering solar-like

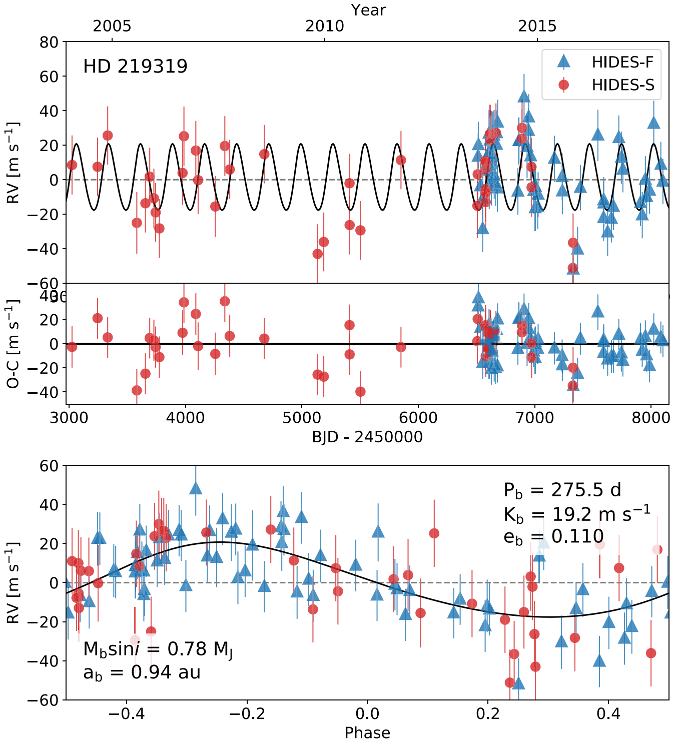

Fig. 30. Orbital solution of HD 219139. HIDES-S data are shown in red circles and HIDES-F data are shown in blue triangles. Top: Best-fitting single Keplerian curve in the full time span, with fitted RV offsets between instruments and fitted jitters included in the error bars. Middle: RV residuals to the best fit. Bottom: Phase-folded of top panel. (Color online)

Table 12. Radial velocities of γ Psc.

BJD (−2450000)	Radial velocity (m s^{-1})	Uncertainty (m s^{-1})	Observation Mode
2489.2149	− 1.4	4.9	HIDES-S
2509.1015	− 2.8	4.4	HIDES-S
2541.1795	12.2	4.3	HIDES-S
2570.0815	− 2.5	4.2	HIDES-S
2652.9006	− 20.8	4.0	HIDES-S
...	...	...	...

*Only the first five sets of RV data are listed. A complete data listing including RV, FWHM, BIS, and *S*/*N* is available online as supplementary data.

oscillations and instrumental jitter, we believe the scatter of rms is acceptable as these rms measurements are located around 20 m s^{-1}.

Appendix 3.9 γ Psc

We collected a total of 89 data including 34 taken by HIDES-S and 55 taken by HIDES-F between 2002 February and 2017 December. The RV data are shown in figure 31 and the data are listed in table 12. The GLS shows a significant peak at the period of 561 d with a FAP of less than 0.1%, and another significant signal located at 224 d. Recognizing the relations of ($1/224 \simeq 1/561 + 1/365$), we know that the 224 d signal is an alias caused by a 1 yr window function. For further investigation of periodicity, we did not find significant periodicity with GLS in line profiles and Ca II H index time series, and we did not find RV strongly correlating with either spectral line profiles or Ca II H index ($|r| < 0.3$).

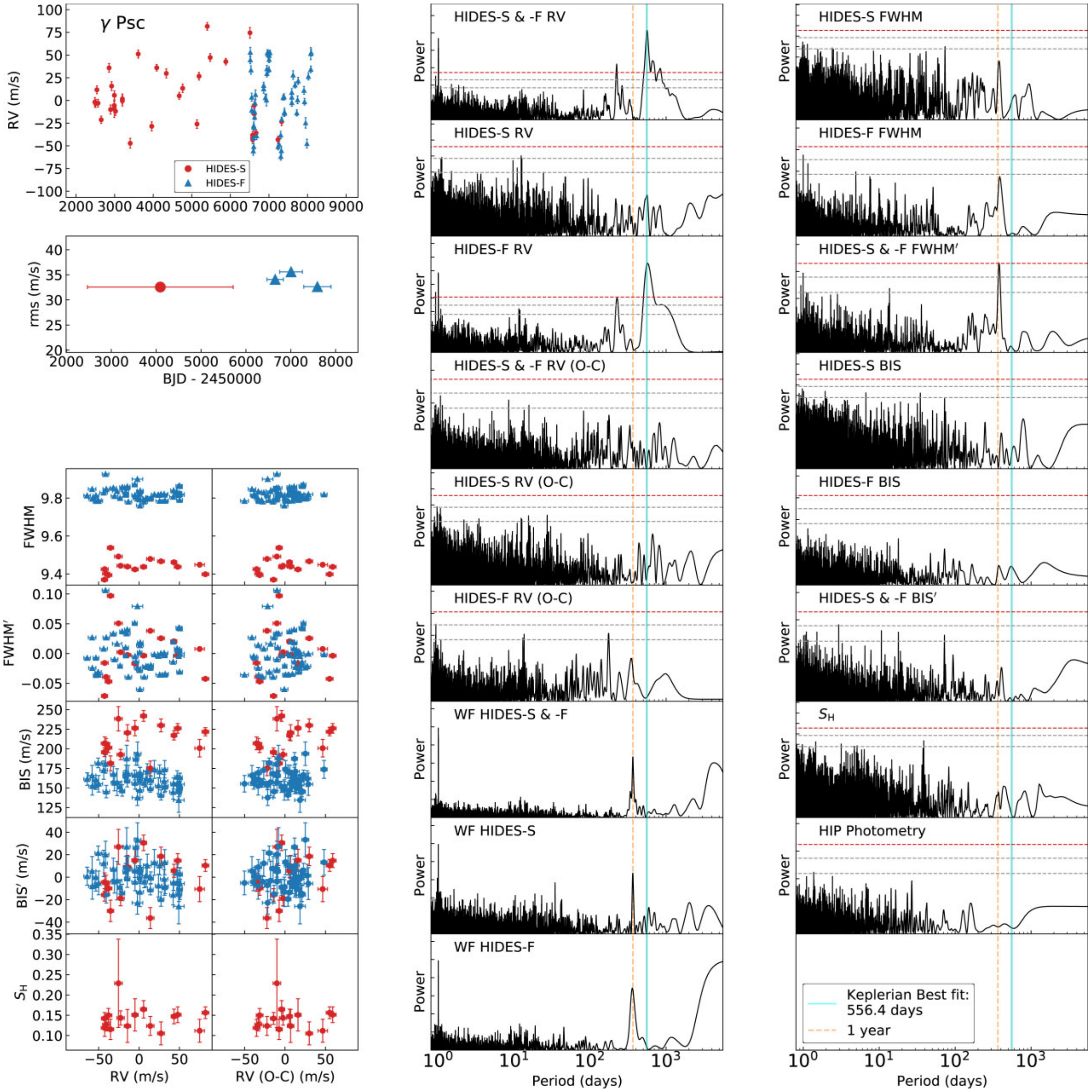

Fig. 31. Summary figure of γ Psc. Left-hand column, from top to bottom: RV time series; rms of RVs varying by time; FWHM, FWHM′, BIS, BIS′, and Ca II H index S_{H}, respectively, against RVs and RV residuals. Middle column, from top to bottom: GLS periodogram of full RV data, HIDES-S RV data, HIDES-F RV data, full RV residuals, HIDES-S RV residuals, and HIDES-F RV residuals; window function of full RV data, HIDES-S data, and HIDES-F data. Right-hand column, from top to bottom: GLS periodogram of HIDES-S FWHM, HIDES-F FWHM, FWHM′, HIDES-S BIS, HIDES-F BIS, BIS′, Ca II H index S_{H}, and Hipparcos photometry. In GLS periodograms, the horizontal lines represent 10%, 1%, and 0.1% FAP level from bottom to top. The vertical cyan solid line indicates the best-fitted period from the Keplerian model, and the vertical orange dashed line indicates 1 yr. (Color online)

We adopted a single Keplerian curve to fit the data and obtained orbital parameters for the companion of $P = 555.1^{+6.0}_{-2.5}$ d, $K = 34.0^{+3.9}_{-5.0}\,\mathrm{m\,s^{-1}}$, and $e = 0.204^{+0.114}_{-0.141}$. The rms scatter of the residuals to the Keplerian fit is $24.6\,\mathrm{m\,s^{-1}}$. We did not find any significant periodicity in the residuals, and we did not find line profiles or Ca II H index strongly correlating with RV residuals ($|r| < 0.4$). Adopting a stellar mass of $M = 0.99\,M_{\odot}$, we obtained a minimum mass $M_{\mathrm{p}} \sin i = 1.34^{+0.02}_{-0.31}\,M_{\mathrm{J}}$ and a semimajor axis $a = 1.32^{+0.05}_{-0.08}$ au for the companion. The phase-folded RV curve is shown in the lower panel in figure 32.

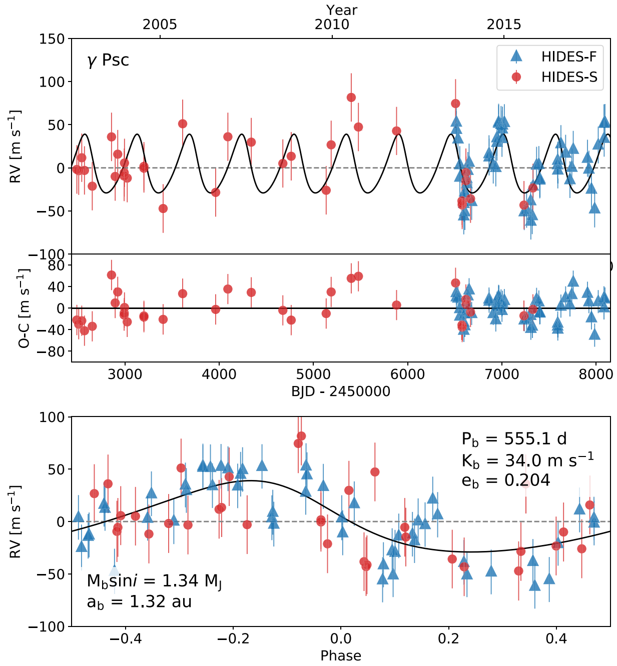

Fig. 32. Orbital solution of γ Psc. HIDES-S data are shown in red circles and HIDES-F data are shown in blue triangles. Top: Best-fitting single Keplerian curve in the full time span, with fitted RV offsets between instruments and fitted jitters included in the error bars. Middle: RV residuals to the best fit. Bottom: Phase-folded of top panel. (Color online)

References

Adamów, M., Niedzielski, A., Kowalik, K., Villaver, E., Wolszczan, A., Maciejewski, G., & Gromadzki, M. 2018, A&A, 613, A47

Adamów, M., Niedzielski, A., Villaver, E., Nowak, G., & Wolszczan, A. 2012, ApJ, 754, L15

Alibert, Y., Mordasini, C., & Benz, W. 2011, A&A, 526, A63

Andrews, S. M., Rosenfeld, K. A., Kraus, A. L., & Wilner, D. J. 2013, ApJ, 771, 129

Baluev, R. V. 2008, MNRAS, 385, 1279

Baranne, A., et al. 1996, A&AS, 119, 373

Barclay, T., Pepper, J., & Quintana, E. V. 2018, ApJS, 239, 2

Berger, T. A., Huber, D., van Saders, J. L., Gaidos, E., Tayar, J., & Kraus, A. L. 2020, AJ, 159, 280

Borucki, W. J., et al. 2012, ApJ, 745, 120

Bovy, J., Rix, H.-W., Green, G. M., Schlafly, E. F., & Finkbeiner, D. P. 2016, ApJ, 818, 130

Butler, R. P., Marcy, G. W., Williams, E., McCarthy, C., Dosanjh, P., & Vogt, S. S. 1996, PASP, 108, 500

Cameron, A. G. W. 1978, Moon Planets, 18, 5

Choi, J., Dotter, A., Conroy, C., Cantiello, M., Paxton, B., & Johnson, B. D. 2016, ApJ, 823, 102

Dall, T. H., Santos, N. C., Arentoft, T., Bedding, T. R., & Kjeldsen, H. 2006, A&A, 454, 341

Döllinger, M. P., & Hartmann, M. 2021, ApJS, 256, 10

Döllinger, M. P., Hatzes, A. P., Pasquini, L., Guenther, E. W., Hartmann, M., Girardi, L., & Esposito, M. 2007, A&A, 472, 649

Dotter, A. 2016, ApJS, 222, 8

Dumusque, X., Udry, S., Lovis, C., Santos, N. C., & Monteiro, M. J. P. F. G. 2011, A&A, 525, A140

Duncan, D. K., et al. 1991, ApJS, 76, 383

ESA 1997, ESA SP-1200, The Hipparcos and Tycho Catalogues (Noordwijk: ESA)

Farr, W. M., et al. 2018, ApJ, 865, L20

Fischer, D. A., & Valenti, J. 2005, ApJ, 622, 1102

Ford, E. B. 2006, ApJ, 642, 505

Foreman-Mackey, D., Agol, E., Ambikasaran, S., & Angus, R. 2017, AJ, 154, 220

Foreman-Mackey, D., Hogg, D. W., Lang, D., & Goodman, J. 2013, PASP, 125, 306

Frink, S., Quirrenbach, A., Fischer, D., Röser, S., & Schilbach, E. 2001, PASP, 113, 173

Fulton, B. J., Petigura, E. A., Blunt, S., & Sinukoff, E. 2018, PASP, 130, 044504

Gaia Collaboration 2016, A&A, 595, A1

Gaia Collaboration 2021, A&A, 649, A1

Gelman, A., et al. 2013, Bayesian Data Analysis, Third Edition (Boca Raton: Chapman and Hall)

Gettel, S., Wolszczan, A., Niedzielski, A., Nowak, G., Adamów, M., Zieliński, P., & Maciejewski, G. 2012, ApJ, 745, 28

Goldreich, P., & Ward, W. R. 1973, ApJ, 183, 1051

Gray, R. O., & Corbally, C. J. 1994, AJ, 107, 742

Green, G. M., Schlafly, E., Zucker, C., Speagle, J. S., & Finkbeiner, D. 2019, ApJ, 887, 93

Grunblatt, S. K., et al. 2017, AJ, 154, 254

Grunblatt, S. K., Howard, A., & Haywood, R. 2016, AAS Meeting, 227, 122.01

Haisch, K. E., Lada, E. A., & Lada, C. J. 2001a, AJ, 121, 2065

Haisch, K. E., Lada, E. A., & Lada, C. J. 2001b, ApJ, 553, L153

Han, I., Lee, B. C., Kim, K. M., Mkrtichian, D. E., Hatzes, A. P., & Valyavin, G. 2010, A&A, 509, A24

Hatzes, A. P., et al. 2018, AJ, 155, 120

Hatzes, A. P., Guenther, E. W., Endl, M., Cochran, W. D., Döllinger, M. P., & Bedalov, A. 2005, A&A, 437, 743

Hayashi, C., Nakazawa, K., & Nakagawa, Y. 1985, in Protostars and Planets II, ed. D. Black & M. Matthews (Tucson: University Arizona Press), 1100

Heeren, P., et al. 2021, A&A, 647, A160

Hekker, S., Reffert, S., Quirrenbach, A., Mitchell, D. S., Fischer, D. A., Marcy, G. W., & Butler, R. P. 2006, A&A, 454, 943

Henry, G. W., Fekel, F. C., Henry, S. M., & Hall, D. S. 2000, ApJS, 130, 201

Huber, D., et al. 2013, Science, 342, 331

Huber, D., et al. 2017, ApJ, 844, 102

Izumiura, H. 1999, in Observational Astrophysics in Asia and its Future, ed. P. S. Chen (Yunnan: Yunnan Observatory), 77

Izumiura, H. 2005, J. Korean Astron. Soc., 38, 8

Jofré, E., Petrucci, R., Saffe, C., Saker, L., Artur de la Villarmois, E., Chavero, C., Gómez, M., & Mauas, P. J. D. 2015, A&A, 574, A50

Johnson, J. A., et al. 2007, ApJ, 665, 785

Johnson, J. A., et al. 2010, ApJ, 721, L153

Johnson, J. A., Marcy, G. W., Fischer, D. A., Henry, G. W., Wright, J. T., Isaacson, H., & McCarthy, C. 2006, ApJ, 652, 1724

Jones, H. R. A., Butler, R. P., Tinney, C. G., Marcy, G. W., Carter, B. D., Penny, A. J., McCarthy, C., & Bailey, J. 2006, MNRAS, 369, 249
Jones, M. I., et al. 2016, A&A, 590, A38
Jones, M. I., Jenkins, J. S., Bluhm, P., Rojo, P., & Melo, C. H. F. 2014, A&A, 566, A113
Jones, M. I., Jenkins, J. S., Rojo, P., & Melo, C. H. F. 2011, A&A, 536, A71
Kambe, E., et al. 2013, PASJ, 65, 15
Kass, R. E., & Raftery, A. E. 1996, J. Am. Statistical Assoc., 90, 773
Kolmogorov, A. 1933, Giornale dell' Istituto Italiano degli Attuari, 4, 83
Kozai, Y. 1962, AJ, 67, 591
Kuiper, G. P. 1951, Proc. Natl. Acad. Sci., 37, 717
Lagrange, A.-M., Desort, M., Galland, F., Udry, S., & Mayor, M. 2009, A&A, 495, 335
Lidov, M. L. 1962, Planet. Space Sci., 9, 719
Lillo-Box, J., et al. 2014, A&A, 562, A109
Lillo-Box, J., Barrado, D., & Correia, A. C. M. 2016, A&A, 589, A124
Lindegren, L., et al. 2021, A&A, 649, A2
Liu, Y. J., Tan, K. F., Wang, L., Zhao, G., Sato, B., Takeda, Y., & Li, H. N. 2014, ApJ, 785, 94
Mason, B. D., Wycoff, G. L., Hartkopf, W. I., Douglass, G. G., & Worley, C. E. 2001, AJ, 122, 3466
Mayor, M., & Udry, S. 2008, Phys. Scr. T, 130, 014010
Medina, A. A., Johnson, J. A., Eastman, J. D., & Cargile, P. A. 2018, ApJ, 867, 32
Mortier, A., & Collier Cameron, A. 2017, A&A, 601, A110
Mortier, A., Faria, J. P., Correia, C. M., Santerne, A., & Santos, N. C. 2015, A&A, 573, A101
Narang, M., Manoj, P., Furlan, E., Mordasini, C., Henning, T., Mathew, B., Banyal, R. K., & Sivarani, T. 2018, AJ, 156, 221
Nelder, J. A., & Mead, R. 1965, Comput. J., 7, 30
Nicholls, C. P., Wood, P. R., Cioni, M.-R. L., & Soszyński, I. 2009, MNRAS, 399, 2063
Niedzielski, A., et al. 2007, ApJ, 669, 1354
Niedzielski, A., et al. 2015, A&A, 573, A36
Niedzielski, A., Nowak, G., Adamów, M., & Wolszczan, A. 2009, ApJ, 707, 768
Paxton, B., et al. 2013, ApJS, 208, 4
Paxton, B., et al. 2015, ApJS, 220, 15
Paxton, B., et al. 2018, ApJS, 234, 34
Paxton, B., Bildsten, L., Dotter, A., Herwig, F., Lesaffre, P., & Timmes, F. 2011, ApJS, 192, 3
Pepe, F., Mayor, M., Galland, F., Naef, D., Queloz, D., Santos, N. C., Udry, S., & Burnet, M. 2002, A&A, 388, 632
Pollack, J. B., Hubickyj, O., Bodenheimer, P., Lissauer, J. J., Podolak, M., & Greenzweig, Y. 1996, Icar, 124, 62
Reffert, S., Bergmann, C., Quirrenbach, A., Trifonov, T., & Künstler, A. 2015, A&A, 574, A116
Reichert, K., Reffert, S., Stock, S., Trifonov, T., & Quirrenbach, A. 2019, A&A, 625, A22
Ribas, Á., Bouy, H., & Merín, B. 2015, A&A, 576, A52
Saar, S. H., Butler, R. P., & Marcy, G. W. 1998, ApJ, 498, L153
Safronov, V. 1969, Evolution of the Protoplanetary Cloud and Formation of the Earth and Planets (Moscow: Nauka)
Saio, H., Wood, P. R., Takayama, M., & Ita, Y. 2015, MNRAS, 452, 3863
Santos, N. C., et al. 2017, A&A, 603, A30
Sato, B., et al. 2012, PASJ, 64, 135
Sato, B., et al. 2013, PASJ, 65, 85
Sato, B., et al. 2015, ApJ, 802, 57
Sato, B., Kambe, E., Takeda, Y., Izumiura, H., & Ando, H. 2002, PASJ, 54, 873
Sato, B., Kambe, E., Takeda, Y., Izumiura, H., Masuda, S., & Ando, H. 2005, PASJ, 57, 97
Schwarz, G. 1978, Ann. Statistics, 6, 461
Setiawan, J., Pasquini, L., da Silva, L., von der Lühe, O., & Hatzes, A. 2003, A&A, 397, 1151
Smirnov, N. 1948, Ann. Math. Statistics, 19, 27
Soszyński, I., et al. 2021, ApJ, 911, L22
Stassun, K. G., Collins, K. A., & Gaudi, B. S. 2017, AJ, 153, 136
Suárez Mascareño, A., et al. 2020, A&A, 639, A77
Takarada, T., et al. 2018, PASJ, 70, 59
Takeda, Y. 1995, PASJ, 47, 287
Takeda, Y., Sato, B., & Murata, D. 2008, PASJ, 60, 781
Takeda, Y., & Tajitsu, A. 2015, MNRAS, 450, 397
Tala Pinto, M., Reffert, S., Quirrenbach, A., Stock, S., Trifonov, T., & Mitchell, D. S. 2020, A&A, 644, A1
Udry, S., et al. 2019, A&A, 622, A37
van Leeuwen, F. 2007, A&A, 474, 653
Winn, J. N., Johnson, J. A., Albrecht, S., Howard, A. W., Marcy, G. W., Crossfield, I. J., & Holman, M. J. 2009, ApJ, 703, L99
Wittenmyer, R. A., et al. 2017b, AJ, 154, 274
Wittenmyer, R. A., Endl, M., Cochran, W. D., & Levison, H. F. 2007, AJ, 134, 1276
Wittenmyer, R. A., Endl, M., Wang, L., Johnson, J. A., Tinney, C. G., & O'Toole, S. J. 2011, ApJ, 743, 184
Wittenmyer, R. A., Jones, M. I., Zhao, J., Marshall, J. P., Butler, R. P., Tinney, C. G., Wang, L., & Johnson, J. A. 2017a, AJ, 153, 51
Wood, P. R., Olivier, E. A., & Kawaler, S. D. 2004, ApJ, 604, 800
Yu, J., Huber, D., Bedding, T. R., & Stello, D. 2018, MNRAS, 480, L48
Zechmeister, M., & Kürster, M. 2009, A&A, 496, 577